



ELSEVIER

Contents lists available at SciVerse ScienceDirect

Signal Processing: *Image Communication*journal homepage: [www.elsevier.com/locate/image](http://www.elsevier.com/locate/image)

# Optical flow estimation in cardiac CT images using the steered Hermite transform

Ernesto Moya-Albor<sup>a,\*</sup>, Boris Escalante-Ramírez<sup>a</sup>, Enrique Vallejo<sup>b</sup><sup>a</sup> Universidad Nacional Autónoma de México, Fac. de Ingeniería, Edif. de Posgrado e Investigación, Ciudad Universitaria, C.P. 04510, México, DF, Mexico<sup>b</sup> Instituto Nacional de Cardiología Ignacio Chávez, Juan Badiano No. 1, Sección XVI, C.P. 14080, México, DF, Mexico

## ARTICLE INFO

## Article history:

Received 31 December 2011

Accepted 13 November 2012

## Keywords:

Optical flow

Differential method

Steered Hermite transform

Steerable filters

Cardiac CT imaging

## ABSTRACT

This paper describes a new method to estimate the heart's motion in computer tomography images with the inclusion of a bio-inspired image representation model. Our proposal is based on the polynomial decomposition of each of the images using the steered Hermite transform as a representation of the local characteristics of images from an perceptual approach within a multiresolution scheme.

The Hermite transform is a model that incorporates some of the more important properties of the first stages of the human visual system, such as the overlapping Gaussian receptive fields, the Gaussian derivative model of early vision and the multi-resolution analysis.

We propose an approach for optical flow estimation that incorporates image structure information extracted from the steered Hermite coefficients, that is later used as local motion constraints in a differential estimation method that involves several of the constraints seen in the current differential methods, which allows obtaining accurate flows.

Considering the importance of understanding the movement of certain structures such as left ventricular and myocardial wall for better medical diagnosis, our main goal is to find an estimation method useful to assist diagnosis tasks in computer tomography images.

© 2012 Elsevier B.V. All rights reserved.

## 1. Introduction

One of the most important advances in diagnostic radiology in recent decades has been the cross-sectional imaging of the human body. After the introduction of computed tomography (CT), ultrasound (US) and magnetic resonance imaging (MRI) diagnostic proposals, treatment and monitoring of disease have changed completely. In particular, spiral computed tomography has become a useful tool for cross-sectional imaging, this due to its robustness, which is moderately invasive and relatively inexpensive. In particular, CT angiography was significantly enhanced by

the rotational speed of the order of sub-seconds and the fineness of the collimation [14].

In a CT, an X-ray beam is rotated rapidly around the patient's body, and the data are transmitted to a computer, where an algorithm assigns to each point (voxel) of a cross section of the image plane a value in a gray scale (Hounsfield unit), indicating the attenuation of the X-rays on tissue. CT images can be enhanced and manipulated in various ways. Generally an ionized contrast agent is injected intravenously during scanning, allowing smaller structures become visible. Moreover, the data can be reconstructed on the computer to provide images through different planes of the body or 3-dimensional images [41].

Computed tomography multislice or multidetector (MSCT) has improved the performance of spiral CT scanners with the introduction of MSCT of 2, 4, 16 and more recently 64-detector elements, where the rotation speed

\* Corresponding author. Tel.: +52 55 56161719.

E-mail addresses: [emoyalbor@gmail.com](mailto:emoyalbor@gmail.com) (E. Moya-Albor), [boris@servidor.unam.mx](mailto:boris@servidor.unam.mx) (B. Escalante-Ramírez), [vallejo.enrique@gmail.com](mailto:vallejo.enrique@gmail.com) (E. Vallejo).

has dropped to less than half a second and the resolution in the sub-millimeter order, allowing scanned large areas in great detail.

The heart has been extensively evaluated radiologically, but mostly in standard two-dimensional images (e.g., X-rays and angiograms of the chest). Standard radiographs of the chest (anterior and posterior) may reveal the silhouette of the heart, as well as the great arteries and pulmonary vasculature, but cannot show small structures and easily determine overlapping structures. MSCT for the evaluation of the heart and coronary arteries was introduced with the generation of 4-row detector instruments in 1999 [14].

Getting a picture of the heart has always been a technical challenge because the heart has a continuous movement. CT images of the heart in motion have been used in the diagnosis with the development of MSCT synchronized with the Electrocardiography (ECG) examination. One of the main advantages of the introduction of MSCT is the speed of acquisition of the images, thus shortening examination of the patient to reduce the amount of contrast required to increase and enhance vascular consistency. The use of MSCT of the heart synchronized with the patient's ECG allows reconstruction of transverse images of the entire cardiac volume during any phase of the cardiac cycle. Usually, the entire stack of images is only reconstructed during diastole to freeze the heart's motion. By performing a reconstruction of the volume during systole and diastole function it is possible to find basic parameters of cardiac function, such as left and right ventricular ejection fraction and the myocardial wall thickness [42].

One problem that has increased worldwide is congestive heart failure, which is due to both left ventricular and right ventricular failure. In the United States, about 5 million patients suffer from this problem and about 500,000 patients develop this condition each year. Previously it was thought that congestive heart failure was due of the left ventricle (LV) to pump blood efficiently (systolic ventricular failure). More recently, there has been emphasis on diastolic ventricular failure, where the systolic function appears to be normal, but diastolic ventricular function is impaired, being the cause of 50% of congestive heart failure in these patients. In order to develop better treatments for congestive heart failure, it is necessary to first understand the basic physiology and movement of both normal and abnormal ventricular relaxation and contraction [13].

Considering the importance of understanding the movement of certain structures such as LV and myocardial wall for better medical diagnosis, this article describes a new method to estimate the heart's motion in computer tomography images. We propose a differential approach to optical flow estimation using the steered Hermite transform, which is a tool that performs a decomposition of the images into visual patterns that are relevant to the human vision system (HSV), such as directional edges, textures, etc. The Hermite transform is an image representation model that mimics some of the more important properties of early vision such as local processing and the Gaussian derivative models of receptive fields [52,32,31].

Although physicians are often interested in the boundaries of structures, our method can also estimate motion

in homogeneous areas that are also of interest for medical diagnosis.

The Hermite transform uses a Gaussian window to extract local information from a image. This information is expanded in terms of a family of orthogonal polynomials. There are reasons why a Gaussian window is used. From a perceptual standpoint the Gaussian window is a good model of the overlapping receptive fields found in physiological experiments [40,26]. According to the scale-space theory, the Gaussian window minimizes the uncertainty product in the spatial and frequency domain [50]. It is also mathematically tractable and there is an approximation of the Gaussian function in the discrete case. The polynomials used to approximate the local information are determined by the analysis window. For the case of a Gaussian window these polynomials involve the Gaussian derivative operators, found in the psychophysical modeling of the HSV [30,7] which provides *natural operators* in agreement with the theory scale-space [25]. In [52–54] it is showed that these functions model the measured receptive field data more accurately than the Gabor functions do, with the additional advantage of being orthogonal at the same location of analysis. Like the receptive fields, both Gabor functions and Gaussian derivatives are spatially local and consist of alternating excitatory and inhibitory regions within a decaying envelope.

A multiresolution decomposition using the Hermite transform can be obtained through a pyramidal scheme [16,44], where the image is decomposed into a number of band-pass or low-pass subimages, which are then subsampled in proportion to their spatial resolution offering a way of relating image structures between different scales. Like [49] where the retinal image is represented through a wavelet-like transform with difference of two Gaussian functions (DoG) as basis filters. We use the Hermite transform for the multiscale decomposition to emulate the behavior of retinal ganglion cell receptive fields that can be described using the DoG at different scales [39]. A multiresolution approach allows using small windows to better detect fine details and large windows to analyze low resolution objects, which is one of the main properties of the HVS.

A rotated version of the Hermite transform provides a very efficient representation of oriented patterns which enables an adaptation to local orientation content at each window position over the image, indicating the direction of one-dimensional pattern. The steered Hermite coefficients are obtained projecting the cartesian Hermite coefficients onto one-dimensional coefficients on an axis that makes an angle  $\theta$  with the  $x$  axis, where the angle  $\theta$  represents the direction of maximum energy. The Hermite filters form a steerable basis because they are products of polynomials with a radially symmetric Gaussian window. Filters of increasing order analyze successively higher radial frequencies and filters of the same order and different (directional) index distinguish between different orientations in the image, which is relevant from a psychophysical approach considering that the HSV calculates Gaussian derivatives at different scales and different directions.

Optical flow estimation methods calculate apparent velocities that can be associated with a variation of brightness

patterns in a sequence of images. In general these methods consider that motion is due to the change in position of different cardiac structures and not due to the relative motion between the observer and the scene or to variations in scene illumination. Many of the differential optical flow approaches are based on the work of Horn and Schunck [24], and Lucas and Kanade [29], which incorporated certain constraints in order to handle the *Ill-posed Opening problem*.

We propose an approach for optical flow estimation that involves several of the constraints seen in the current differential methods, which allows obtaining an accurate optical flow [11,12,38]. We use local image constraints as mentioned in [24,38] and assume that the flow is piecewise smooth as in [10–12]. Similarly to [6,12], the proposed optimization function is robust to outliers and a multiresolution strategy was implemented to handle large displacements as mentioned in [6,2,33,34].

Our contribution includes local restrictions using the steered Hermite transform as a representation of the local image characteristics from an perceptual approach. In [38] the effect of different local restrictions on the data term (intensity, gradient, Hessian, Laplacian) is described, but in our approach the steered Hermite coefficients allow including polynomial decomposition of the image and take these parameters as constraints that include intensity and higher order derivatives, which are useful to analyze the image in a similar way as is done by the HSV. The use of Gaussian derivatives allows incorporating image structure information from neighboring pixels that is robust to noise [29,5]. This feature is incorporated in a global differential functional that allows obtaining dense flow fields [24,35].

The nature of CT images compels the estimation of optical flow algorithms to be robust in noisy environments, this complicates the accurate calculation of the derivatives used in classical differential methods that usually uses a smoothing prefilter. Using Gaussian derivatives the estimation is more robust to noise because the smoothing is implicitly included in the proposed functional applied at different scales of analysis.

In order to expose the patient to less radiation CT cardiac images are captured in a few discrete times of the cardiac cycle. Therefore there are large displacements of the structures between two consecutive images. Including a Gaussian window in the polynomial decomposition of the Hermite transform allows incorporating information from neighboring pixels that helps finding optical flow in areas that change dramatically from one image to another. Moreover the inclusion of a multiresolution analysis in the proposed functional also helps dealing with large displacements. In this sense, motion discontinuities are also dealt with using filters similar to those found in HSV.

In summary, our proposal includes a multiresolution HSV-inspired perspective to optical flow estimation in CT images. The steered Hermite transform extracts the local image characteristics, that are later used as motion constraints in a differential estimation method, which allows obtaining accurate flows.

This paper is structured as follows. In Section 2 we present the theory and the mathematical foundations of the Hermite transform, which allows to consider the Hermite transform as a good model for describing the images. In Section 3 we

introduce the rotated version of the Hermite transform, which allows locally adapting the analysis to representative visual patterns. Related work and elements of the state of the art of optical flow estimation are shown in Section 4. Section 5 presents our method differential optical flow estimation using the steered Hermite coefficients as the main tool of analysis, which includes elements that allow obtaining a robust optical flow in a perceptual framework. The results obtained are reported in Section 6 and conclusions are given in Section 7. Appendix A provides a proof for a Hermite transform property that allows us to simplify the solution of the proposed functional. Finally, some simplifications of the numerical solution are show in Appendices B and C.

## 2. The Hermite transform as a model of image representation

The Hermite transform [32,31] is a special case of polynomial transform, it can be considered as an image description model. In order to calculate the Hermite transform, the original image  $L(x,y)$  (where  $(x,y)$  are the coordinates of the pixels) is located at various positions multiplying  $L(x,y)$  by the window function  $v^2(x-x_0,y-y_0)$  at positions  $(x_0,y_0)$  that conform the sampling lattice  $S$

$$L_v(x-x_0,y-y_0) = L(x,y)v^2(x-x_0,y-y_0) \quad (1)$$

By replicating the window function over the sampling lattice, we can define a weight function different from zero for all  $(x,y)$

$$V(x,y) = \sum_{(x_0,y_0) \in S} v^2(x-x_0,y-y_0) \quad (2)$$

Therefore the original image is represented within the window by

$$L(x,y) = \frac{1}{V(x,y)} \sum_{(x_0,y_0) \in S} L(x,y)v^2(x-x_0,y-y_0) \quad (3)$$

The local information for each analysis window  $L_v(x-x_0,y-y_0)$  is expanded in terms of a family of orthogonal polynomials  $G_{m,n-m}(x,y)$  of  $m$  degree in  $x$  and  $(n-m)$  in  $y$

$$\begin{aligned} L_{m,n-m}(x_0,y_0) \\ = \int_{-\infty}^{\infty} \int_{-\infty}^{\infty} [L(x,y)v^2(x-x_0,y-y_0)]G_{m,n-m}(x-x_0,y-y_0) dx dy \end{aligned} \quad (4)$$

The polynomials  $G_{m,n-m}(x,y)$  used to approximate the information within the window are determined by the analysis window and satisfy the orthogonality condition

$$\int_{-\infty}^{\infty} \int_{-\infty}^{\infty} v^2(x,y)G_{m,n-m}(x,y)G_{l,k-l}(x,y) dx dy = C_{nk}\delta_{nk}\delta_{ml} \quad (5)$$

for  $n,k=0, \dots, \infty$ ,  $m=0, \dots, n$  and  $l=0, \dots, k$ ; where  $\delta_{nk}$  denotes the Kronecker function ( $\delta_{nk} = 1$  for  $n=k$  and  $\delta_{nk} = 0$  for  $n \neq k$ ). The polynomials are orthonormal after a normalization by the factor  $C_{nk}$  or when  $C_{nk} = 1$ .

For example, for a decomposition up to order  $N=2$  where  $N$  is the polynomial degree, we have that  $n=0, 1, \dots, N$  and  $m=0, \dots, n$  are the indexes of the polynomials used in the decomposition as defined in Table 1.

We mentioned above that the polynomials  $G_{m,n-m}(x,y)$  are orthogonal with respect to the window function.

From a perceptual standpoint and according to the scale-space theory, our option would be a Gaussian window

$$v(x,y) = \frac{1}{\sigma\sqrt{\pi}} \exp\left(-\frac{(x^2+y^2)}{2\sigma^2}\right) \quad (6)$$

where the normalization factor defines a unitary energy for  $v^2(x,y)$ .

The reasons why a Gaussian window is of interest are numerous. First, the theory related to the Gaussian function is mathematically tractable. In addition, there is discrete approximation of the Gaussian function, which is useful for implementation purposes. Secondly, adjacent Gaussian windows separated by twice the standard deviation  $\sigma$  are a good model of overlapping receptive fields found in physiological experiments [40,26]. Third, a signal decomposition into orthogonal polynomials with respect to the Gaussian window involves Gaussian derivative operators, which are found in the psychophysical modeling of the HSV [30,7,52–54]. Finally, the Gaussian window minimizes the product of uncertainty in the spatial and frequency domains [50].

With a Gaussian window function, the associated orthogonal polynomials are the Hermite polynomials [45]

$$G_{m,n-m}(x,y) = \frac{1}{\sqrt{2^n m!(n-m)!}} H_m\left(\frac{x}{\sigma}\right) H_{n-m}\left(\frac{y}{\sigma}\right) \quad (7)$$

where  $H_n(x)$  denotes the  $n$ th Hermite polynomial given by Rodrigues's formula [1]

$$H_n(x) = (-1)^n \exp^{x^2} \frac{d^n}{dx^n} \exp^{-x^2} \quad (8)$$

Substituting  $G_{\sigma^2}(x)$  (with variance  $\sigma^2$ ) by  $\exp^{-x^2/\sigma^2}$  in Eq. (8), we obtain the generalized Hermite polynomials with respect to the Gaussian function  $G_{\sigma^2}(x)$

$$H_n\left(\frac{x}{\sigma}\right) = (-1)^n G_{\sigma^2}^{-1}(x) \frac{d^n}{dx^n} G_{\sigma^2}(x) \quad (9)$$

Thus, from Eq. (4) the polynomial coefficients  $L_{m,n-m}(x,y)$  are calculated by a convolution of the original image  $L(x,y)$  with the filter function  $D_{m,n-m}(x,y)$ , followed by a subsampling ( $T$ ) at position  $(x_0,y_0)$  of the sampling lattice  $S$

$$L_{m,n-m}(x_0,y_0) = \int_{-\infty}^{\infty} \int_{-\infty}^{\infty} L(x,y) D_{m,n-m}(x-x_0,y-y_0) dx dy \quad (10)$$

$n = 0, 1, \dots, \infty$   
 $m = 0, 1, \dots, n$

where  $D_{m,n-m}(x,y) = G_{m,n-m}(-x,-y)v^2(-x,-y)$ ,  $L_{m,n-m}$  are the Hermite coefficients, and  $(n-m)$  and  $m$  denote the analysis order in  $x$  and  $y$  direction, respectively. In Fig. 1 we show the analysis process of the Hermite transform.

**Table 1**

Indexes of the polynomials used in a decomposition of order  $N=2$  ( $n=0,1,\dots,N$  and  $m=0,\dots,n$ ).

$n$	$m = 0, 1, \dots, n$	$G_{m,n-m}(x,y)$
$n=0$	$m=0$	$G_{0,0-0}(x,y) = G_{0,0}(x,y)$
$n=1$	$m=0$	$G_{0,1-0}(x,y) = G_{0,1}(x,y)$
	$m=1$	$G_{1,1-1}(x,y) = G_{1,0}(x,y)$
$n=2$	$m=0$	$G_{0,2-0}(x,y) = G_{0,2}(x,y)$
	$m=1$	$G_{1,2-1}(x,y) = G_{1,1}(x,y)$
	$m=2$	$G_{2,2-2}(x,y) = G_{2,0}(x,y)$

In Fig. 2 we show a typical graphical distribution of the Hermite coefficients in function of the order of the polynomials in the  $x$  and  $y$  directions.

The filter function  $D_{m,n-m}(x,y)$  are separable because the Gaussian window is rotationally symmetric, therefore

$$D_{m,n-m}(x,y) = D_m(x)D_{n-m}(y) \quad (11)$$

The Hermite filters can be computed by

$$D_n(x) = \frac{(-1)^n}{\sqrt{2^n n!}} \cdot \frac{1}{\sigma\sqrt{\pi}} H_n\left(\frac{x}{\sigma}\right) \exp^{-x^2/\sigma^2} \quad (12)$$

The analysis functions of the Hermite transform are similar to Gaussian derivatives, which, as argued before, are good models of some of the important retinal and cortical cells of the HSV. They model filter operations in human vision with the same accuracy as the Gabor filters, with the advantage that they accomplish this task with fewer parameters [32,52,54]. Fig. 3 shows the Hermite filters  $D_n(x)$  for  $N=4$  ( $n=0, 1, 2, 3, 4$ ).

Fig. 5 shows the slice 52 of the CT sequence at 20% of the cardiac cycle and in Fig. 6 we obtain the cartesian Hermite coefficients for  $N=3$  ( $n=0, 1, 2, 3$ ).

In order to recover the original image an interpolation of the transform coefficients with the synthesis filters  $P_{m,n-m}(x,y)$  is performed followed by an oversampling and adding all the elements

$$\hat{L}(x,y) = \sum_{n=0}^{\infty} \sum_{m=0}^n \sum_{(x_0,y_0) \in S} L_{m,n-m}(x_0,y_0) P_{m,n-m}(x-x_0,y-y_0) \quad (13)$$

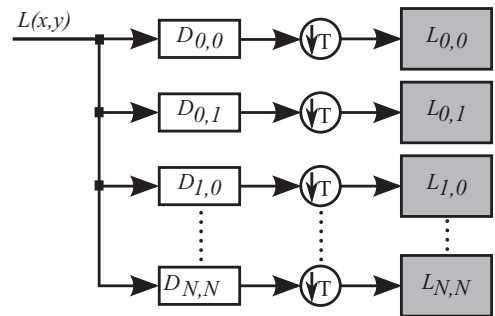


**Fig. 1.** Analysis process of the Hermite transform.

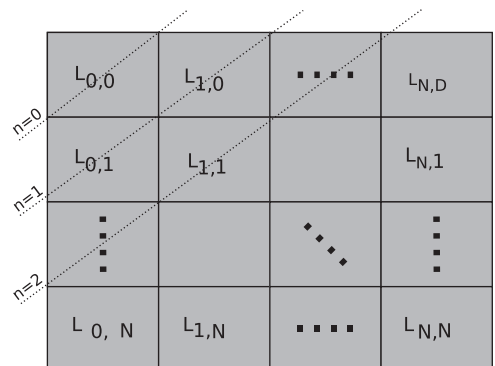


**Fig. 2.** Typical graphical distribution of the Hermite coefficients.

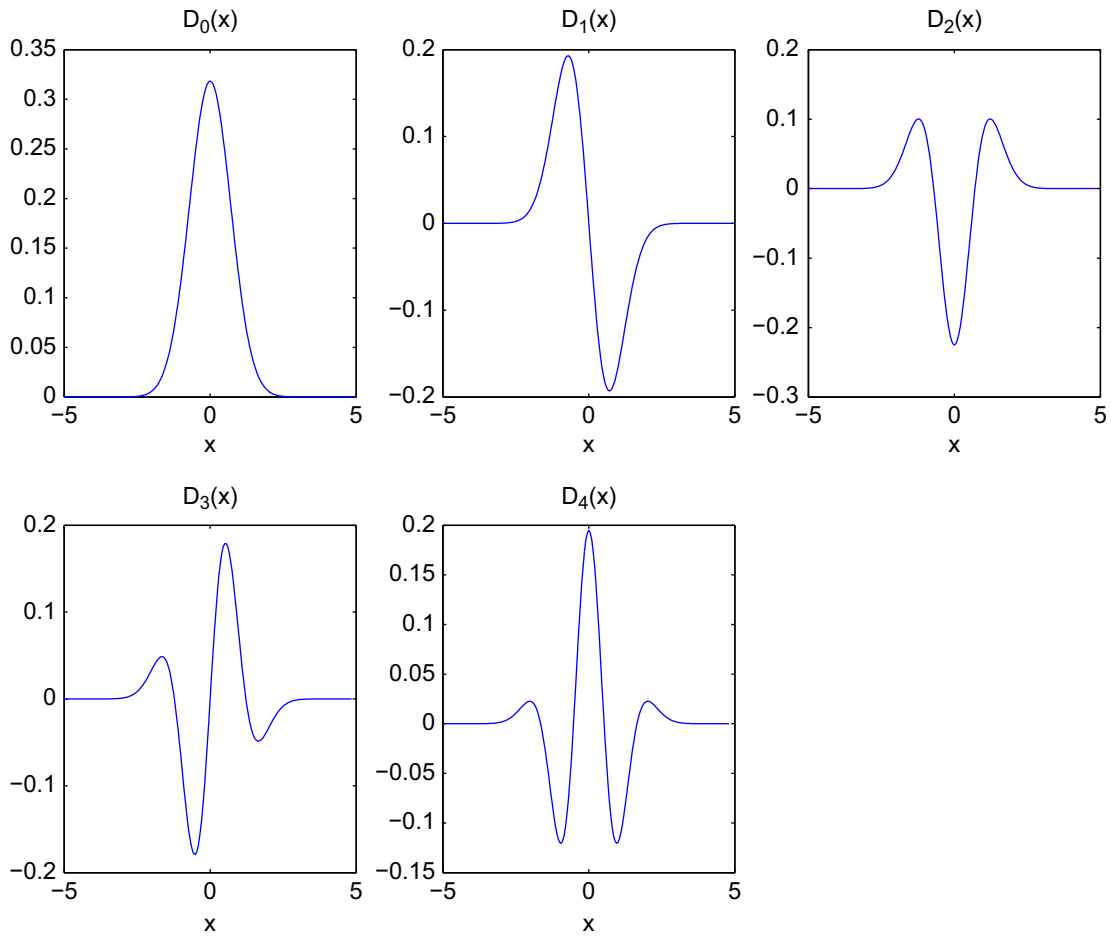


Fig. 3. The Hermite filters  $D_n(x)$  for  $N=4$  ( $n=0, 1, 2, 3, 4$ ).

where

$$P_{m,n-m}(x,y) = \frac{G_{m,n-m}(x,y)v^2(x,y)}{V(x,y)} \quad (14)$$

for  $n=0, \dots, \infty$  and  $m=0, \dots, n$ . In Fig. 4 we show the synthesis process of the Hermite transform.

The free parameters of the Hermite transform are the maximum derivative order  $N$ , the subsampling factor and the scale  $\sigma$  which must be related to the spatial scale of the image structures to be analyzed. Small windows are better to detect fine details and large windows allow analyzing low resolution objects. The Hermite transform has a multiresolution extension that allows analyzing objects at different scales [16,44].

### 3. Steered Hermite transform

Oriented filters are a class of filters that are rotated copies of each filter, constructed as a linear combination of a set of basis filters [20]. The orientation feature of the Hermite filters explains why they are products of polynomials with a radially symmetric window function (Gaussian function). The  $N+1$  Hermite filters of order  $n$  form a steerable basis for each individual filter of order  $n$ .

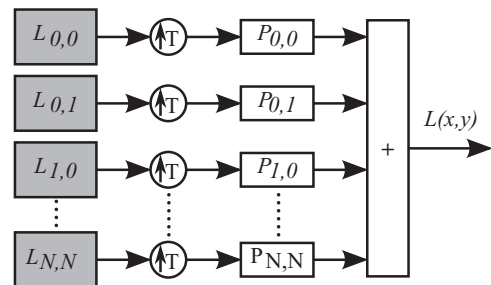


Fig. 4. Synthesis process of the Hermite transform.

Because of this characteristic, Hermite filters at each position in the image are adapted to local content [48]. The resulting filters can be interpreted as directional derivatives of a Gaussian function.

For orientation analysis purposes, it is convenient to work with a rotated version of the Hermite transform. The polynomial coefficients can be computed through a convolution of the image with the filter functions  $D_m(x)D_{n-m}(y)$ . They are separable in space and polar domains, and its Fourier transform can be expressed in

polar coordinates. If  $\omega_x = \omega \cos(\theta)$  and  $\omega_y = \omega \sin(\theta)$ , then  $d_m(\omega_x)d_{n-m}(\omega_y) = g_{m,n-m}(\theta) \cdot d_n(\omega)$  (15)

where  $d_n(\omega)$  is the Fourier transform of each filter function, which expresses radial frequency selectivity of the  $n$ th derivative of the Gaussian but with a radial coordinate  $r$  for  $x$

$$d_n(\omega) = \frac{1}{\sqrt{2^n n!}} (-j\omega\sigma)^n \exp\left(-\frac{(\omega\sigma)^2}{4}\right) \quad (16)$$

and  $g_{m,n-m}(\theta)$  expresses the directional selectivity of the filter.

$$g_{m,n-m}(\theta) = \sqrt{\binom{n}{m}} \cos^m \theta \cdot \sin^{n-m} \theta \quad (17)$$

Filters of increasing order  $n$  analyze successively higher radial frequencies and filters of the same order  $n$  and different (directional) index  $m$  distinguish between different orientations in the image [32]. Note that the radial frequency selectivity  $d_n(\omega)$  is the same for all  $N+1$  filters of the order  $n$  and that these filters differ only in their orientation selectivity. In terms of orientation frequency functions, this property of the Hermite filters can be expressed by

$$g_{m,n-m}(\theta - \theta_0) = \sum_{k=0}^n l_{k,n-k,\theta_0}(x,y) \cdot g_{k,n-k}(\theta) \quad (18)$$

where  $l_{k,n-k,\theta_0}(x,y)$  are the steered Hermite coefficients. The Hermite filter rotation at each position over the image is an adaptation to local orientation content.

In order to obtain the steered Hermite coefficients, the Hermite coefficients are rotated toward the estimated local orientation, according to a criterion of maximum oriented energy at each window position. For local 1D patterns, the steered Hermite transform provides a very efficient representation. This representation consists of a parameter  $\theta$  that indicates the orientation of the pattern and a small number of coefficients that represent the profile of the pattern

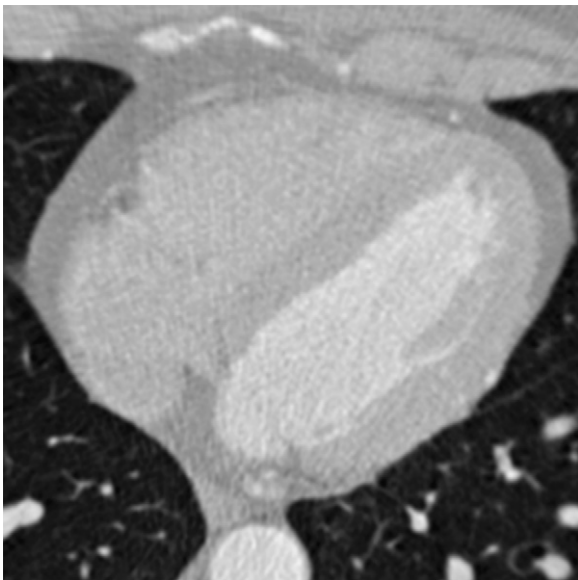


Fig. 5. Slice 52 of the CT sequence at 20% of the cardiac cycle.

perpendicular to its orientation. For a 1D pattern with orientation  $\theta$ , the following relation holds:

$$l_{m,n-m,\theta}(x,y) = \begin{cases} \sum_{k=0}^n L_{k,n-k}(x,y) \cdot g_{k,n-k}(\theta), & m=0 \\ 0, & m>0 \end{cases} \quad (19)$$

For such pattern, steering over  $\theta$  results in a compaction of energy into the coefficients  $l_{0,n,\theta}(x,y) = l_{n,\theta}(x,y)$ , while all other coefficients are set to zero.

Using Hermite coefficients, the energy content can be expressed according to Parseval Theorem as

$$E_N = \sum_{n=0}^N \sum_{m=0}^n [L_{m,n-m}(x,y)]^2 \quad (20)$$

up to order  $N$ .

The steered Hermite transform offers a way to describe 1D patterns on the basis of their orientation and profile. We can differentiate 1D energy terms and 2D energy terms. That is, for each local signal:

$$E_N^{1D} = \sum_{n=1}^N [l_{0,n,\theta}(x,y)]^2 \quad (21)$$

$$E_N^{2D} = \sum_{n=0}^N \sum_{m=0}^n [l_{m,n-m,\theta}(x,y)]^2 \quad (22)$$

where the energy content of Eq. (20) can be expressed as

$$E_N = [L_{0,0}(x,y)]^2 + E_N^{1D} + E_N^{2D} \quad (23)$$

In Fig. 7 we steer the cartesian Hermite coefficients of Fig. 6 according to maximum energy direction, the angle  $\theta$  was estimated using the phase of the gradient, which is a good indicator of the direction of the edges, for this we use the coefficients  $L_{01}$  and  $L_{10}$

$$\theta(x,y) = \arctan \frac{L_{0,1}(x,y)}{L_{1,0}(x,y)} \quad (24)$$

where  $L_{01}$  and  $L_{10}$  are a good approach to optimal edge detectors in the horizontal and vertical directions, respectively.

It is noticeable that the energy is concentrated in only three coefficients (Fig. 7(b)–(d)), which represent the orientation of the different structures of the image.

## 4. Differential methods of optical flow estimation

### 4.1. Notation used in the equations

Let  $L(x,y,t)$  be a image sequence, where  $(x,y)$  represents the location within a rectangular image domain  $\Omega$ , and  $t \in [0, \tau]$  denotes time. Let  $u$  and  $v$  be the displacement of a pixel at position  $(x,y)$  within the sequence of images at a time  $t$  to a time  $(t+1)$  in the directions  $x$  and  $y$ , respectively.

We define the following relations:

$$W = (u, v, 1)^T, \quad |\nabla W|^2 = |\nabla u|^2 + |\nabla v|^2, \quad |\nabla_3 W|^2 = |\nabla_3 u|^2 + |\nabla_3 v|^2$$

$$\nabla u = (u_x, u_y)^T, \quad \nabla_3 u = (u_x, u_y, u_t)^T, \quad X = (x, y, t)^T$$

$$L_* = \frac{\partial L}{\partial \mathbf{x}}, \quad \nabla_3 L = (L_x, L_y, L_t)^T$$

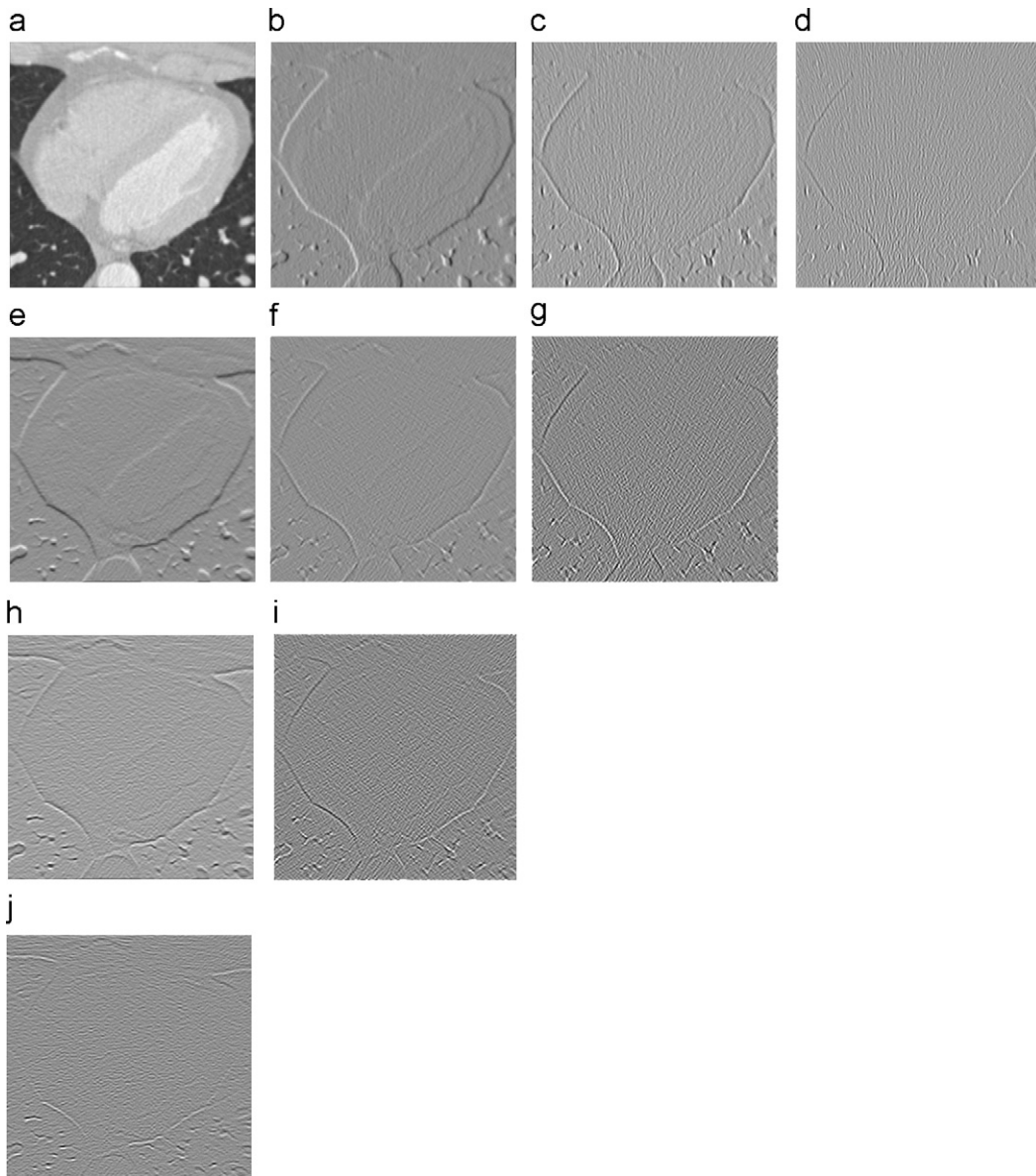


**Fig. 6.** Cartesian Hermite coefficients slice 52 of the CT sequence at 20% of the cardiac cycle for  $N=3$  ( $n=0, 1, 2, 3$ ). (a)  $L_{0,0}(x,y)$  (represents the DC Hermite coefficient). (b)  $L_{1,0}(x,y)$ . (c)  $L_{2,0}(x,y)$ . (d)  $L_{3,0}(x,y)$ . (e)  $L_{0,1}(x,y)$ . (f)  $L_{1,1}(x,y)$ . (g)  $L_{2,1}(x,y)$ . (h)  $L_{0,2}(x,y)$ . (i)  $L_{1,2}(x,y)$ . (j)  $L_{0,3}(x,y)$ .

#### 4.2. Related work

The optical flow can be defined as 2D distribution of apparent velocities that can be associated with a variation of brightness patterns in a sequence of images [22,23]. It can be represented by a vector field induced by the motion of objects (or camera), which encodes the displacement of each pixel in the image.

To detect the optical flow in cardiac CT images taken at different times of the cardiac cycle, we consider that the movement is due to the change in position of different cardiac structures and not due to the relative motion between the observer and the scene or to the variations in scene illumination as is the case of synthetic images.

Many of the methods of differential optical flow estimation are based on the work of [24] and [29], which incorporated certain restrictions in order to handle the *Ill-posed Opening Problem*. In recent years, different approaches have emerged that have suggested some additional restrictions to overcome these problems [10,9,12,38]:

- Local image restrictions.
- Statistical robust optimization functions.
- Spatial coherence.

##### 4.2.1. Local image restrictions

Horn and Schunck [24] assume that the intensities of the pixels of the objects remain constant. *Constant Intensity*

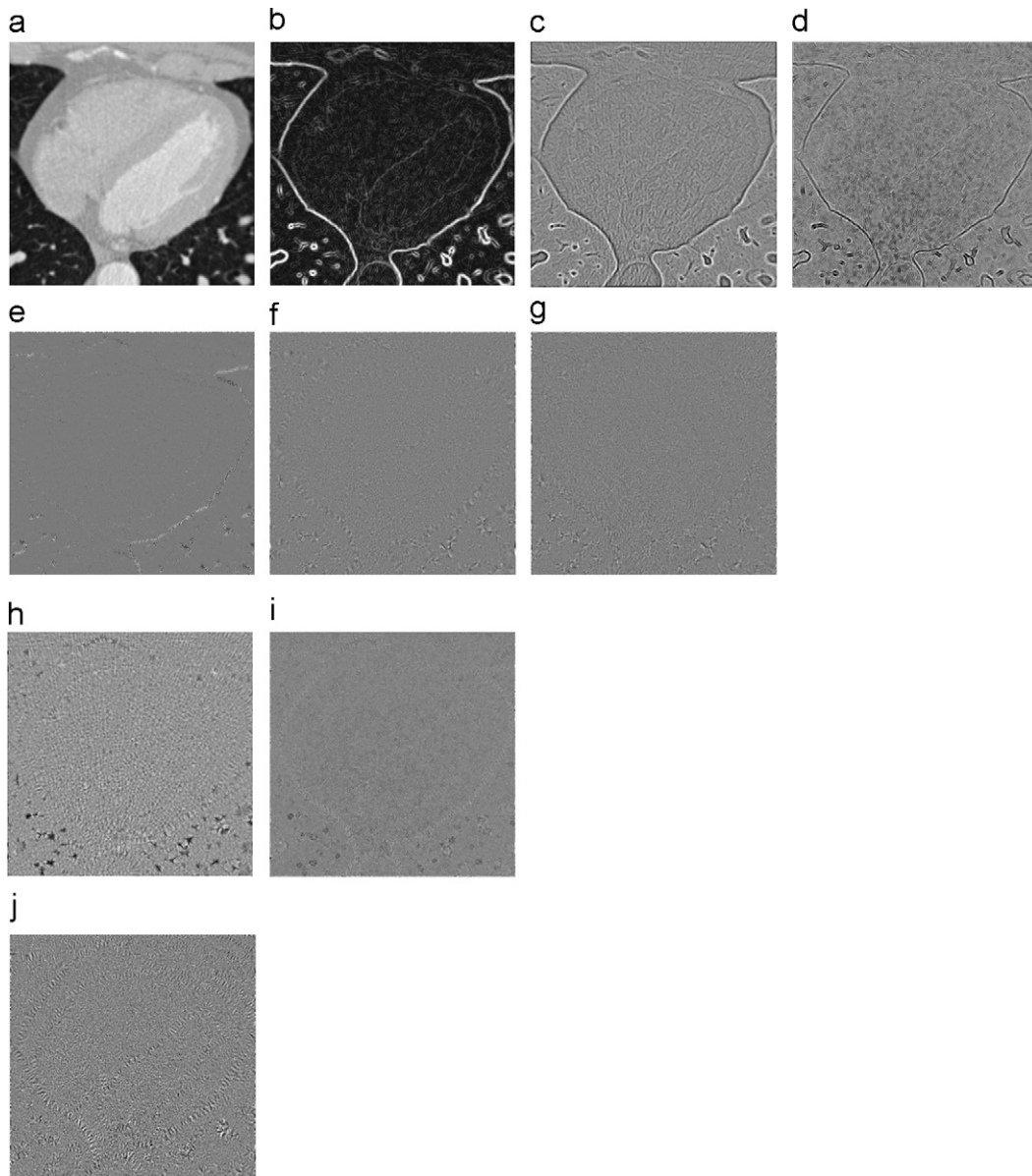


**Fig. 7.** Steered Hermite coefficients of slice 52 of the CT sequence at 20% of the cardiac cycle for  $N=3$  ( $n=0,1,2,3$ ). (a)  $l_{0,0}(x,y)$  (represents the DC Hermite coefficient). (b)  $l_{1,0,\theta}(x,y)$ . (c)  $l_{2,0,\theta}(x,y)$ . (d)  $l_{3,0,\theta}(x,y)$ . (e)  $l_{0,1,\theta}(x,y)$ . (f)  $l_{1,1,\theta}(x,y)$ . (g)  $l_{2,1,\theta}(x,y)$ . (h)  $l_{0,2,\theta}(x,y)$ . (i)  $l_{1,2,\theta}(x,y)$ . (j)  $l_{0,3,\theta}(x,y)$ .

#### Constraint

$$L(x+u,y+v,t+1)-L(x,y,t)=0 \quad (25)$$

Considering linear displacements, we can expand Eq. (25) by Taylor's series obtaining the *Optical Flow Constraint* equation

$$W^T(\nabla_3 L)=0 \quad (26)$$

In order to minimize Eq. (26), [29] considers the flow constant within a neighborhood  $\rho$  (Gaussian function  $K_\rho$ ). Letting determine the two constants  $u$  and  $v$  at a point

$(x,y,t)$  using a weighted least squares approach

$$E_{LK}^2(W)=W^T J_\rho(\nabla_3 L)W \quad (27)$$

The intensity does not always remain constant from one image to another, therefore an independent intensity change measure is required. In [35,36] a *Constant Gradient Constraint* (generally used in local methods to handle the aperture problem) is proposed

$$\nabla L(x+u,y+v,t+1)-\nabla L(x,y,t)=0 \quad (28)$$

The disadvantages of considering only local restrictions are observed in homogeneous areas where movement is

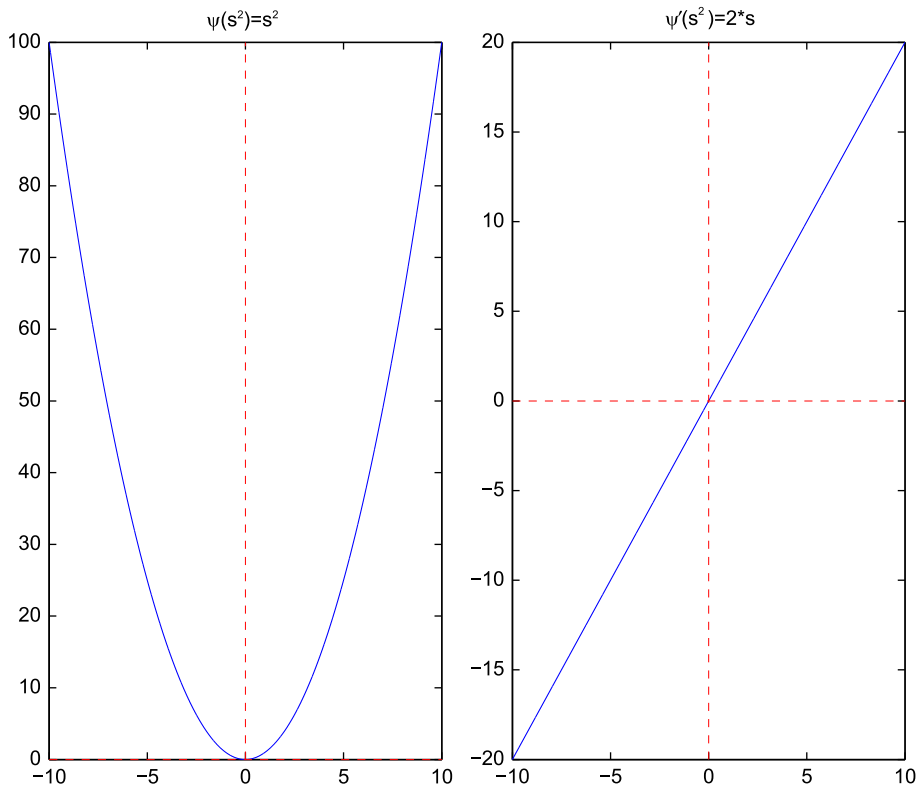


Fig. 8.  $l^2$  norm :  $\Psi(s^2) = s^2$ .

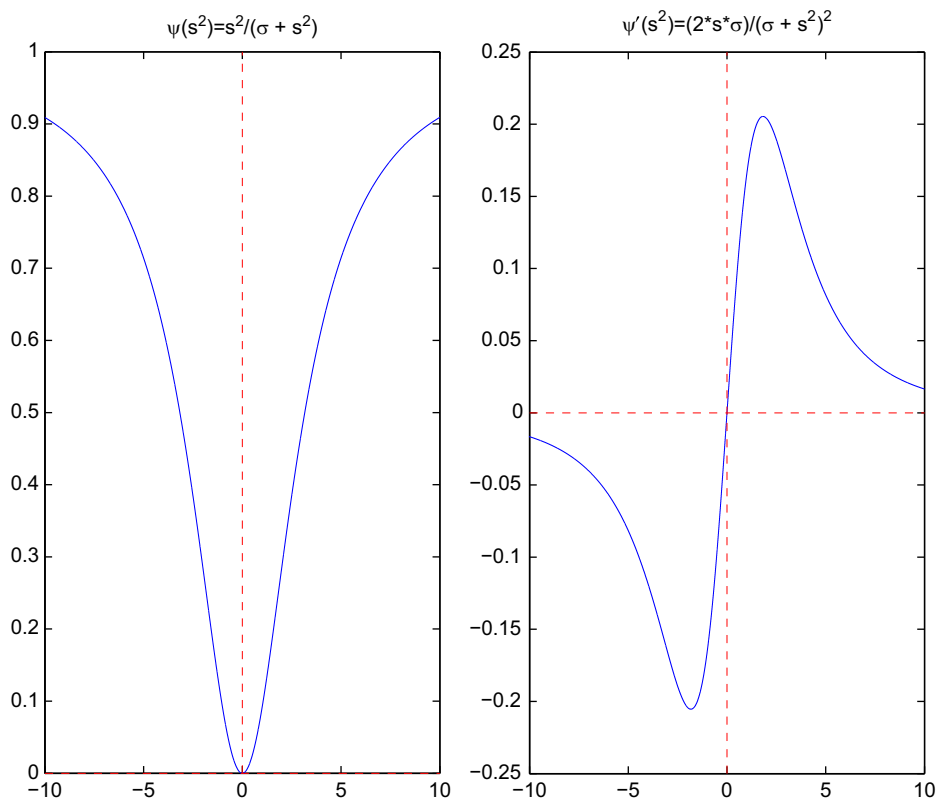


Fig. 9. Geman-MacClure norm :  $\Psi(s^2) = s^2 / (\sigma + s^2)$ , with scaling parameter  $\sigma = 10$ .

observed locally and only the normal component of the movement can be estimated (aperture problem). An additional restriction is therefore required. In [24] it is assumed that the apparent speed of the intensity pattern in the image varies smoothly, that is, neighboring points of the objects have similar velocities, *Smoothness Constraint*

$$E_{HS}^2(W) = \int_{\Omega} (W^T J_0(\nabla_3 L)W + \alpha |\nabla W|^2) dX \quad (29)$$

where  $\alpha$  is a regularization parameter.

The smoothness term can get information from neighbors in regions where the intensity gradient is zero, resulting in dense flow fields and making unnecessary interpolation stages commonly found in local differential methods. In this context, [10–12] proposed a combination of local and global estimation, combining the robustness against noise of the local differential approaches as in Eq. (27) [29,5] and dense flow fields of global differential methods as in Eq. (29) [24,35] and defining a Combined Local-Global (CLG) method

$$E_{CLG}^2(W) = \int_{\Omega} (W^T J_{\rho}(\nabla_3 L)W + \alpha |\nabla W|^2) dX \quad (30)$$

In order to improve robustness to noise, a space-time formulation, performing a convolution with a three-dimensional Gaussian function and considering soft flows

in the temporal direction was made by [11]

$$E_{CLG3}^2(W) = \int_{\Omega \times [0, \tau]} (W^T J_{\rho}(\nabla_3 L)W + \alpha |\nabla_3 W|^2) dX \quad (31)$$

4.2.2. Statistical robust optimization functions

Eqs. (27) and (29) use quadratic optimization  $\Psi(s^2) = s^2$  ( $\ell^2$  norm) to assign considerable weight to outliers. This is shown in its associated influence function ( $\Psi' = \partial \Psi(s^2) / \partial s$ ), which increases linearly and without borders (Fig. 8). On the other hand  $\ell^1$  norm has a constant value in its influence function but it is used to a lesser extent because of the complexity to minimize the functional.

Optimization functions more lenient with respect to outliers and with influence functions tending to zero, should be considered, e.g., the Geman–MacClure (Fig. 9) and Lorentzian influence functions [6,12].

A non-linear approach to Eq. (31) is defined by [12]

$$E_{CLG3-N}^2(W) = \int_{\Omega \times [0, \tau]} (\Psi_1(W^T J_{\rho}(\nabla_3 L)W) + \alpha \Psi_2(|\nabla_3 W|^2)) dX \quad (32)$$

with Charbonnier optimization function [15]

$$\Psi_i(s^2) = 2\beta_i^2 \sqrt{\left(1 + \frac{s^2}{\beta_i^2}\right)} \quad (33)$$

$i = 1, 2$

where  $\beta$  is a scaling parameter.

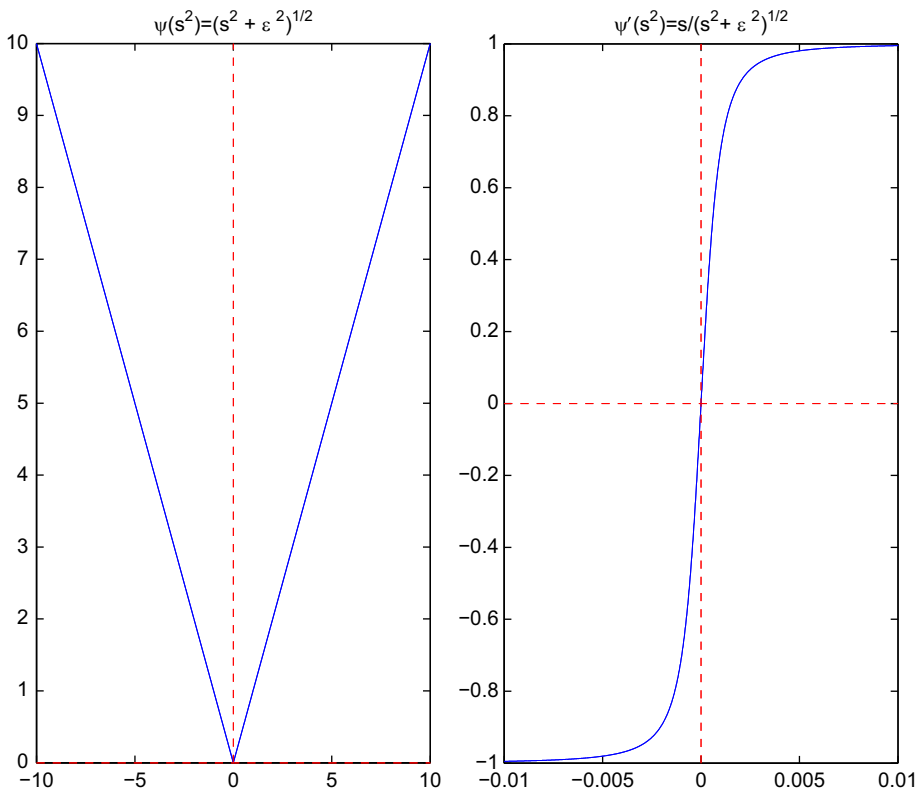


Fig. 10. Modified  $\ell^1$  norm:  $\Psi(s^2) = \sqrt{(s^2 + \epsilon^2)}$ ,  $\epsilon = 0.001$ .

4.2.3. Spatial coherence

The *Uniform Smoothness Constraint* used in [24] causes an over-smoothing at borders of objects. The modified  $\ell^1$  norm or *Flow-driven Isotropic Regularization* is robust in the presence of flow discontinuities as presented in [6,12] (Fig. 10)

$$\min \int_{\Omega} \Psi(\nabla|u|^2 + \nabla|v|^2)$$

$$\Psi(s^2) = \sqrt{(s^2 + \epsilon^2)} \tag{34}$$

where  $\epsilon$  ensures the differentiability of  $\Psi(s^2)$  in  $s=0$ , so that it is chosen reasonably small, for example  $\epsilon \approx 0.001$  [38].

An approach taking into account the occlusions was proposed by [51] which uses bilateral filtering [46] in space, intensity and flow.

The equation of *Optical Flow Constraint* is valid when the displacements are relatively small. In order to handle large displacements multiresolution strategies are used [6,2,33,34]. In this context, [12] proposes a functional where the estimated flow in a coarse resolution is used to correct (*warping*) the original sequence before going to the next finer level. In this way, it creates a hierarchy of problems, where only small displacements are calculated at each stage.

The final displacement field is most accurate in comparison with the linearization of the *Optical Flow Constraint*. The non-linear CLG multiscale approach is given by

$$E_{CLG3-N}^m(\delta W^m) = \int_{\Omega \times [0, \tau]} (\Psi_1(\delta W^{mT} J_{\rho}(\nabla_3 L(X + W^m)) \delta W^m) + \alpha \Psi_2(|\nabla_3(W^m + \delta W^m)|^2)) dX \tag{35}$$

where  $W^{m+1} = W^m + \delta W^m$  and  $\delta W^m$  denotes the motion increment at resolution level  $m$ , with  $m=0$  being the coarsest level with initialization  $w^0 = (0,0,0)$ . The penalty function  $\Psi_i$  is given by Eq. (33).

Papenberg et al. [38] propose a functional that combines *Constant Intensity Constraint* [36], *Constant Gradient Constraint* [47], *Spatio-temporal Smoothness Constraint* and

multiscale approach (*warping*)

$$E_{Warp}(u, v) = \int_{\Omega \times [0, \tau]} \Psi(|L(X+W) - L(X)|^2 + \gamma |\nabla L(X+W) - \nabla L(X)|^2) dX + \alpha \int_{\Omega \times [0, \tau]} \Psi(|\nabla_3 u|^2 + |\nabla_3 v|^2) dX \tag{36}$$

where  $\Psi(s^2) = \sqrt{(s^2 + \epsilon^2)}$  which yields the total variation regularize and  $\gamma$  is a weight between the *Constant Intensity Constraint* and the *Constant Gradient Constraint*.

5. Optical flow estimation using the steered Hermite transform

There have been previous approaches to motion estimation based on the Hermite transform. Liu et al. [28] propose a method that includes a spatio-temporal filtering using the Hermite transform and generalized motion models, such as the affine model, into a single spatial scale. This scheme is proposed the classical *Constant Intensity Constraint* of [24] considering small displacements. More recently, in [43] a directional energy was defined in terms of the 1D Hermite transform coefficients of local projections. Each projection was described by the Hermite transform in terms of a directional derivative analysis of the input at a given scale. The Hermite transform coefficients were then used to detect 1D or 2D spatio-temporal patterns within the 3D stack of images. In [17], a spatio-temporal energy based method to estimate motion in an image sequences was presented. A directional energy was defined in terms of the Radon projections of the Hermite transform. The Radon transform provides a suitable representation for image orientation analysis, while the Hermite transform describes image features locally in terms of Gaussian derivatives. A directional response derived from the directional energy is then used to estimate local motion as well as to compute a confidence matrix. This matrix is used to propagate the velocity information toward directions with high uncertainty.

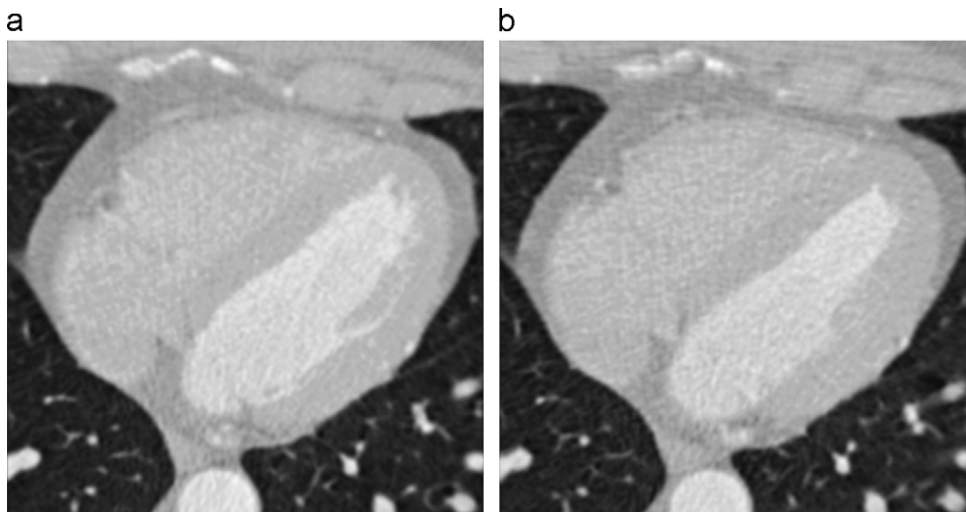
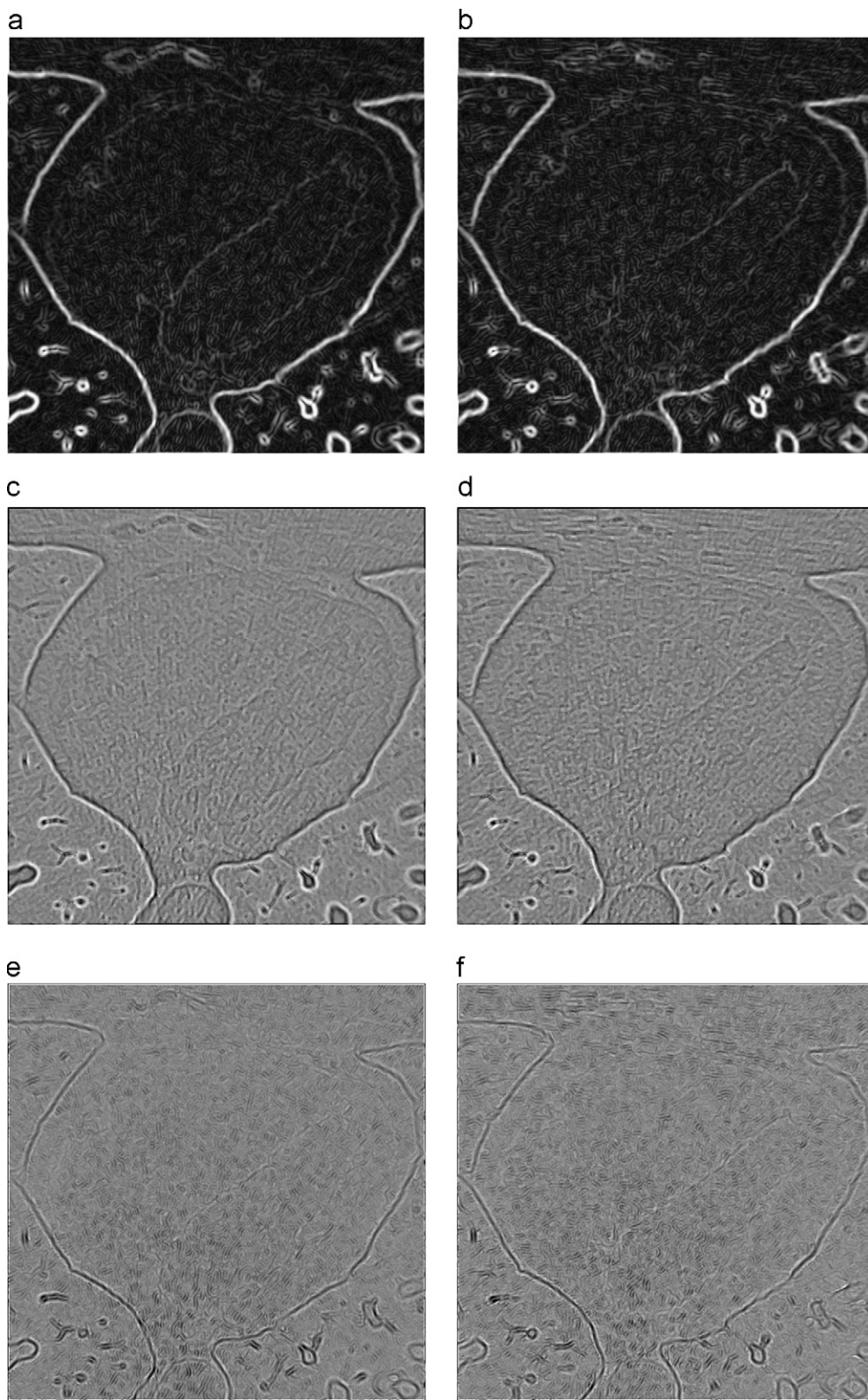


Fig. 11. Cartesian Hermite coefficients  $L_{00}$  of slice 52 of the CT sequence at 20% and 30% of the cardiac cycle. (a)  $L_{0,0}(x,y,t)$ . (b)  $L_{0,0}(x+u,y+v,t+1)$ .



**Fig. 12.** Steered Hermite coefficients up to order  $N=3$  of slice 52 of the CT sequence at 20% and 30% of the cardiac cycle. (a)  $l_{1,\theta}(x,y,t)$ . (b)  $l_{1,\theta}(x+u,y+v,t+1)$ . (c)  $l_{2,\theta}(x,y,t)$ . (d)  $l_{2,\theta}(x+u,y+v,t+1)$ . (e)  $l_{3,\theta}(x,y,t)$ . (f)  $l_{3,\theta}(x+u,y+v,t+1)$ .

Unlike the above methods of optical flow estimation using the Hermite transform [28,43,17], the present proposal poses a differential approach to estimation. It has been show that differential methods offer better optical flow estimation [4,21].

5.1. Model

Given two consecutives images  $L(x,y,t)$  and  $L(x+u, y+v,t+1)$  in a short period of time, our proposal is based on the polynomial decomposition of each of the images using the steered Hermite transform as a representation of the local characteristics of images from an perceptual approach within a multiresolution scheme. We include elements found in recent advances of differential methods which allow obtaining an accurate optical flow [11,12,38].

5.1.1. Constancy assumptions

In [38] the effect of different local image restrictions [24] on the data terms (intensity, gradient, Hessian, Laplacian) of the differential methods are described. Our contribution includes a polynomial decomposition of the image and takes as local restrictions the zero order coefficient of the Hermite transform which represents the intensity of the image and the directional higher order derivatives implicitly contained in the steered Hermite coefficients to analyze the image in a similar way as it is done in the HSV. The use of the derivatives of a Gaussian function allows incorporating information from neighboring pixels to determine the local image constraints, similar to local differential methods, as described in Eq. (27) which are robust to noise [29,5]. This feature is included in a global differential functional in order to obtain dense flow fields as in [24,35].

The local image restrictions of our proposal are

• *Constant Intensity Constraint*

The coefficient of order 0 of the Hermite transform  $L_{0,0}$  ( $L_0$  for simplicity) contains a smoothed version of the original image, so it can be used to define the *Constant Intensity Constraint*

$$L_0(x,y,t) = L_0(x+u,y+v,t+1) \tag{37}$$

where the smoothing implicit in the DC coefficient allows eliminate any component of high frequency noise inherent in the CT images. Fig. 11

shows the coefficients  $L_0$  of slice 52 of the CT sequence at 20% and 30% of the cardiac cycle, where there is a displacement  $(u,v)$  of the pixels in the position  $(x,y)$  of a time  $t$  to a time  $(t+1)$ .

• *Steered Hermite Coefficient Constraint*

A global change of intensity of the images on two consecutive times violates the *Constant Intensity Constraint* but not the gradient of the images, which is only affected in the magnitude but not in its direction. Moreover, in [38] the *Constant Gradient Constraint* considers higher order derivatives for the formulation of constancy assumptions such as the constancy of the Hessian, the constancy of the Laplacian, the constancy of the norm of the Hessian and the constancy of the determinant of the Hessian. It is mentioned that derivatives of order larger than two can also be

considered. Therefore in our proposal we include the steered Hermite coefficients  $l_{n,\theta}$  up to order  $N$  for dealing with various movements, such as translational and rotational motions. This allows including higher derivatives simply by changing the maximum order  $N$  of the decomposition of the Hermite transform.

In this sense we define the *Steered Hermite Coefficient Constraint*:

$$l_{n,\theta}(x,y,t) = l_{n,\theta}(x+u,y+v,t+1) \tag{38}$$

where  $n = 1, 2, \dots, N$  and  $\theta$  is the angle of maximum energy for the position  $(x,y)$ , which is given by Eq. (24). Using the steered Hermite coefficients we obtain rotation invariance as demonstrated in [18]. This allows defining local image restrictions considering constancy in the polynomial decomposition of images and identifying perceptually relevant visual patterns that represent the most important characteristics of the image.

Fig. 12 shows the coefficients  $l_{n,\theta}$  of slice 52 of the CT sequence at 20% and 30% of the cardiac cycle.

• *Smoothness Constraint*:

We assume that the flow is piecewise smooth as in [10–12] allowing to have robustness to discontinuities of flow

$$\min \int_{\Omega} \Psi(|\nabla u|^2 + |\nabla v|^2) dX \tag{39}$$

where  $\Psi(s^2)$  is a non-quadratic penalty function which enables capture also locally non-smooth motion, allowing outliers in the smoothness assumption.

5.1.2. Energy

We define a functional that penalizes deviations from model assumptions. All deviations from the assumption of *Constant Intensity Constraint* (Eq. (37)), *Steered Hermite Coefficient Constraint* (Eq. (38)) and *Smoothness Constraint* (Eq. (39)) are measured by the energy

$$E(u,v) = E_{Data}(u,v) + \alpha E_{Smooth}(u,v) \tag{40}$$

where the regularization parameter  $\alpha > 0$  is a smoothness weight.

The data term  $E_{Data}(u,v)$  is given by

$$E_{Data}(u,v) = \int_{\Omega} \Psi(|L_0(X+W) - L_0(X)|^2 + \gamma |l_{n,\theta}(X+W) - l_{n,\theta}(X)|^2) dX \tag{41}$$

**Table 2**  
Optical flow parameters using steered Hermite transform approach.

Parameter name	Symbol	Value
Hermite Polynomial degree	$N$	3
Downsampling factor	$\eta$	0.95
Regularization parameter	$\alpha$	50
Local constraint weight	$\gamma$	90
Decomposition levels	$M$	40
Outer iteration number	$k$	15
Inner iteration number	$l$	50

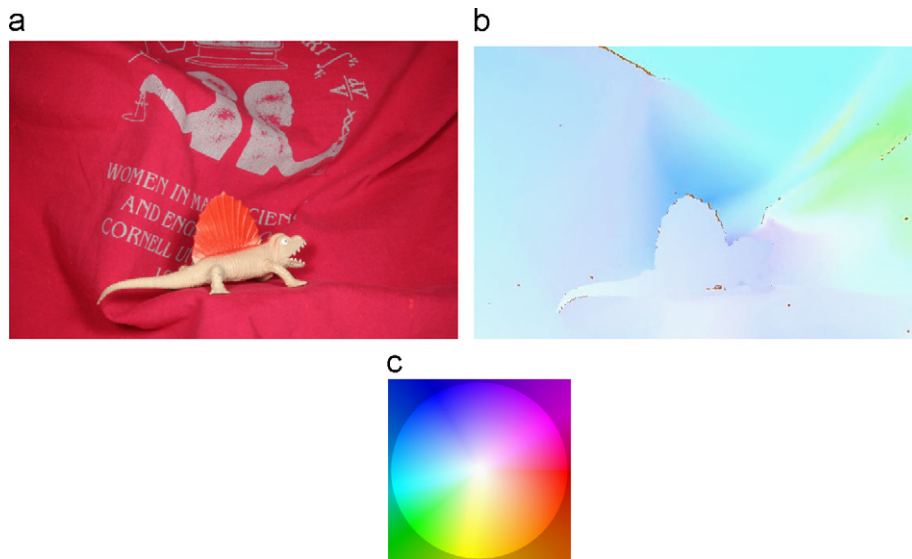


**Fig. 13.** Optical flow of the sequence *Dimetrodon*. (a) Frame 10 of the sequence. (b) *Ground truth*. (c) Reference color wheel.

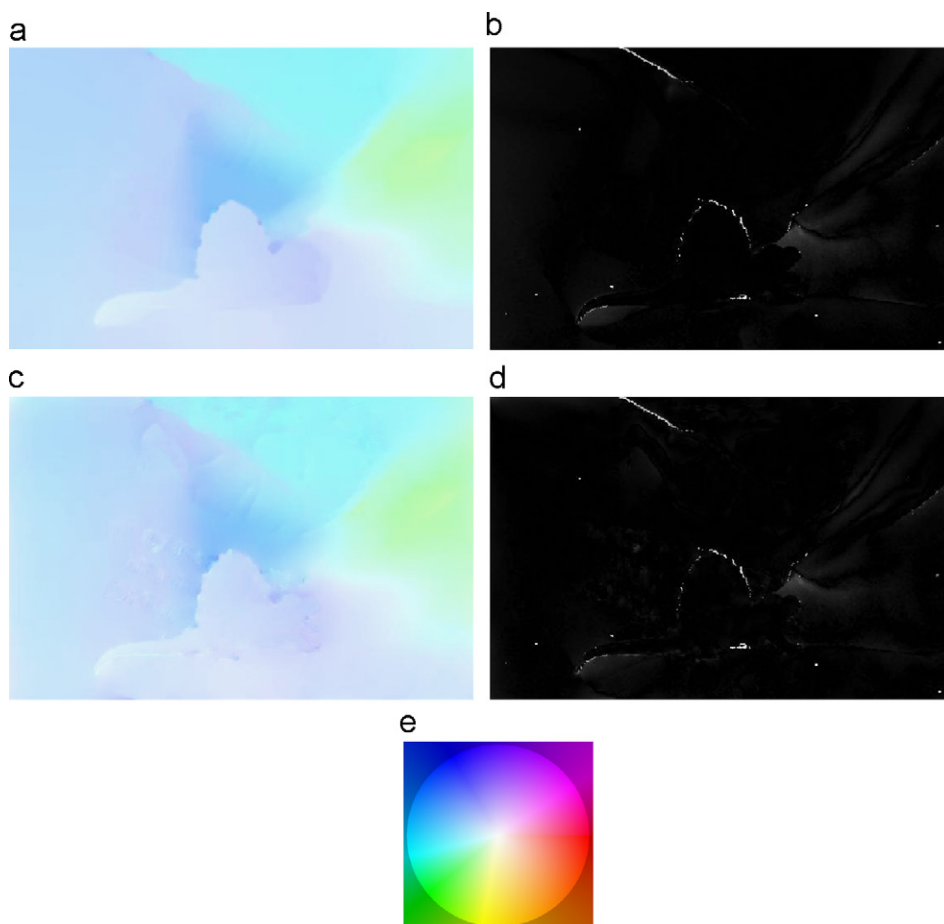


**Fig. 14.** Optical flow fields of the *Dimetrodon* sequence. (a) Optical flow approach of [38]. (b) Absolute error between the *ground truth* and the optical flow approach of [38]  $AE = 3.03^\circ$ . (c) Optical flow using the steered Hermite coefficients. (d) Absolute error between the *ground truth* and the optical flow using steered Hermite coefficients  $AE = 2.7^\circ$ . (e) Reference color wheel.

where  $\gamma$  is a weight between the *Constant Intensity Constraint* and the *Steered Hermite Coefficient Constraint*.

As optimization function we use the modified  $\ell^1$  norm (Eq. (34)), which is robust to outliers:

$$\Psi(s^2) = \sqrt{(s^2 + \epsilon^2)} \quad (42)$$

where  $\epsilon = 0.001$  ensure the differentiability of  $\Psi(s^2)$  in  $s=0$ .

We include the smoothness term of Eq. (39)

$$E_{Smooth}(u, v) = \int_{\Omega} \Psi(|\nabla u|^2 + |\nabla v|^2) dX \quad (43)$$

Therefore our global energy functional to minimize that includes the data and smoothness term has the form

$$E(u, v) = \int_{\Omega} \Psi(|L_0(X+W) - L_0(X)|^2 + \gamma |l_{n,\theta}(X+W) - l_{n,\theta}(X)|^2) dX + \alpha \int_{\Omega} \Psi(|\nabla u|^2 + |\nabla v|^2) dX \quad (44)$$

The proposed functional, includes the coefficient of order 0 ( $n=0$ ) and the steered Hermite coefficients of the Hermite transform as basic elements to define the local image restrictions through a polynomial decomposition of degree  $N$  ( $n = 1, 2, \dots, N$ ).

### 5.2. Numerical solution

The corresponding Euler–Lagrange equations that satisfy the minimization of Eq. (44) in function of  $W$  are

$$\Psi'(|L_0(X+W) - L_0(X)|^2 + \gamma |l_{n,\theta}(X+W) - l_{n,\theta}(X)|^2) \times [ |L_0(X+W) - L_0(X)| L_{10}(X+W) + \gamma ( |l_{n,\theta}(X+W) - l_{n,\theta}(X)| l_{n,\theta_{(m)+1}}(X+W) ) ] - \alpha \operatorname{div}(\Psi'(|\nabla u|^2 + |\nabla v|^2) \nabla u) = 0 \quad (45)$$

$$\Psi'(|L_0(X+W) - L_0(X)|^2 + \gamma |l_{n,\theta}(X+W) - l_{n,\theta}(X)|^2) \times [ |L_0(X+W) - L_0(X)| L_{01}(X+W) + \gamma ( |l_{n,\theta}(X+W) - l_{n,\theta}(X)| l_{n,\theta_{(m)+1}}(X+W) ) ] - \alpha \operatorname{div}(\Psi'(|\nabla u|^2 + |\nabla v|^2) \nabla v) = 0 \quad (46)$$

For a description of the simplification procedure see [Appendix B](#).

#### 5.2.1. Iterative approach

Defining a fixed-point iterative scheme, as in [38], to find a solution for  $W$  in Eqs. (45) and (46), leads to the following equations:

$$\Psi'(|L_0(X+W^{k+1}) - L_0(X)|^2 + \gamma |l_{n,\theta}(X+W^{k+1}) - l_{n,\theta}(X)|^2) \times [ |L_0(X+W^{k+1}) - L_0(X)| L_{10}(X+W^k) + \gamma ( |l_{n,\theta}(X+W^{k+1}) - l_{n,\theta}(X)| l_{n,\theta_{(m)+1}}(X+W^k) ) ] - \alpha \operatorname{div}(\Psi'(|\nabla u^{k+1}|^2 + |\nabla v^{k+1}|^2) \nabla u^{k+1}) = 0 \quad (47)$$

$$\Psi'(|L_0(X+W^{k+1}) - L_0(X)|^2 + \gamma |l_{n,\theta}(X+W^{k+1}) - l_{n,\theta}(X)|^2) \times [ |L_0(X+W^{k+1}) - L_0(X)| L_{01}(X+W^k) + \gamma ( |l_{n,\theta}(X+W^{k+1}) - l_{n,\theta}(X)| l_{n,\theta_{(m)+1}}(X+W^k) ) ] - \alpha \operatorname{div}(\Psi'(|\nabla u^{k+1}|^2 + |\nabla v^{k+1}|^2) \nabla v^{k+1}) = 0 \quad (48)$$

where  $W^k = (u^k, v^k, 1)^T$  are the unknown variables  $u^k$  and  $v^k$  in the outer iteration  $k$ , thus  $W^{k+1}$  is the solution for Eqs. (47) and (48).

Eqs. (47) and (48) are non-linear in the terms of the form  $f(X+W^{k+1}) - f(X)$ , therefore we use a first order Taylor expansion of such terms (see [Appendix C](#)). The resulting equation system reads

$$\Psi'(|L_0(X+W^k) - L_0(X)| + du^k L_{10}(X+W^k) + dv^k L_{01}(X+W^k))^2 + \gamma ( |l_{n,\theta}(X+W^k) - l_{n,\theta}(X)| + du^k l_{n,\theta_{(m)+1}}(X+W^k) + dv^k l_{n,\theta_{(m)+1}}(X+W^k) )^2 [ |L_0(X+W^k) - L_0(X)| L_{10}(X+W^k) + \gamma ( |l_{n,\theta}(X+W^k) - l_{n,\theta}(X)| + du^k l_{n,\theta_{(m)+1}}(X+W^k) + dv^k l_{n,\theta_{(m)+1}}(X+W^k) ) ] - \alpha \operatorname{div}(\Psi'(|\nabla(u^k + du^k)|^2 + |\nabla(v^k + dv^k)|^2) \nabla(u^k + du^k)) = 0 \quad (49)$$

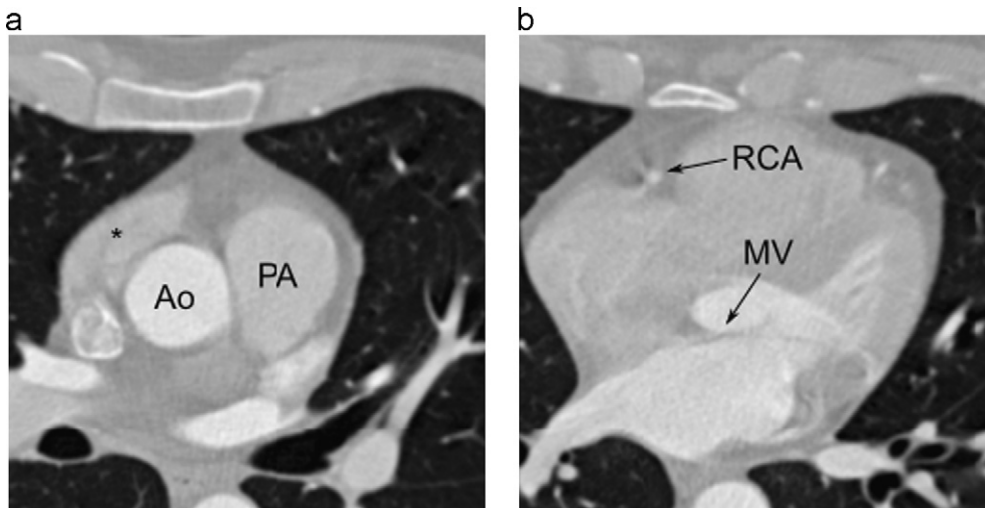


**Fig. 15.** Axial anatomy of the heart. (a) Sample of the right atrial appendage, the ascending aorta and pulmonary artery (\*, Ao and PAPA, respectively). (b) Sample of the right coronary artery and the mitral valve (RCA and MV).

$$\begin{aligned}
& \Psi'(|L_0(X+W^k)-L_0(X)+du^kL_{10}(X+W^k)+dv^kL_{01}(X+W^k)|^2 \\
& +\gamma|I_{n,\theta}(X+W^k)-I_{n,\theta}(X)+du^kI_{n,\theta(m)+1}(X+W^k) \\
& +dv^kI_{n,\theta(m)+1}(X+W^k)|^2[|L_0(X+W^k)-L_0(X) \\
& +du^kL_{10}(X+W^k)+dv^kL_{01}(X+W^k)|L_{01}(X+W^k) \\
& +\gamma(|I_{n,\theta}(X+W^k)-I_{n,\theta}(X)+du^kI_{n,\theta(m)+1}(X+W^k) \\
& +dv^kI_{n,\theta(m)+1}(X+W^k)|I_{n,\theta(m)+1}(X+W^k))] \\
& -\alpha \operatorname{div}(\Psi'(|\nabla(u^k+du^k)|^2+|\nabla(v^k+dv^k)|^2) \\
& \nabla(v^k+dv^k))=0 \tag{50}
\end{aligned}$$

In order to remove the non-linearity in  $\Psi'$  we apply a second fixed-point iteration, with index  $l$  for the inner iteration

$$\begin{aligned}
& \Psi'(|L_0(X+W^k)-L_0(X)+du^{k,l}L_{10}(X+W^k)+dv^{k,l}L_{01}(X+W^k)|^2 \\
& +\gamma|I_{n,\theta}(X+W^k)-I_{n,\theta}(X)+du^{k,l}I_{n,\theta(m)+1}(X+W^k) \\
& +dv^{k,l}I_{n,\theta(m)+1}(X+W^k)|^2[|L_0(X+W^k)-L_0(X) \\
& +du^{k,l+1}L_{10}(X+W^k)+dv^{k,l+1}L_{01}(X+W^k)|L_{10}(X+W^k) \\
& +\gamma(|I_{n,\theta}(X+W^k)-I_{n,\theta}(X)+du^{k,l+1}I_{n,\theta(m)+1}(X+W^k) \\
& +dv^{k,l+1}I_{n,\theta(m)+1}(X+W^k)|I_{n,\theta(m)+1}(X+W^k))] \\
& -\alpha \operatorname{div}(\Psi'(|\nabla(u^k+du^{k,l})|^2+|\nabla(v^k+dv^{k,l})|^2) \\
& \nabla(u^k+du^{k,l+1}))=0 \tag{51}
\end{aligned}$$

$$\begin{aligned}
& \Psi'(|L_0(X+W^k)-L_0(X)+du^{k,l}L_{10}(X+W^k)+dv^{k,l}L_{01}(X+W^k)|^2 \\
& +\gamma|I_{n,\theta}(X+W^k)-I_{n,\theta}(X)+du^{k,l}I_{n,\theta(m)+1}(X+W^k) \\
& +dv^{k,l}I_{n,\theta(m)+1}(X+W^k)|^2[|L_0(X+W^k)-L_0(X) \\
& +du^{k,l+1}L_{10}(X+W^k)+dv^{k,l+1}L_{01}(X+W^k)|L_{01}(X+W^k) \\
& +\gamma(|I_{n,\theta}(X+W^k)-I_{n,\theta}(X)+du^{k,l+1}I_{n,\theta(m)+1}(X+W^k) \\
& +dv^{k,l+1}I_{n,\theta(m)+1}(X+W^k)|I_{n,\theta(m)+1}(X+W^k))]
\end{aligned}$$

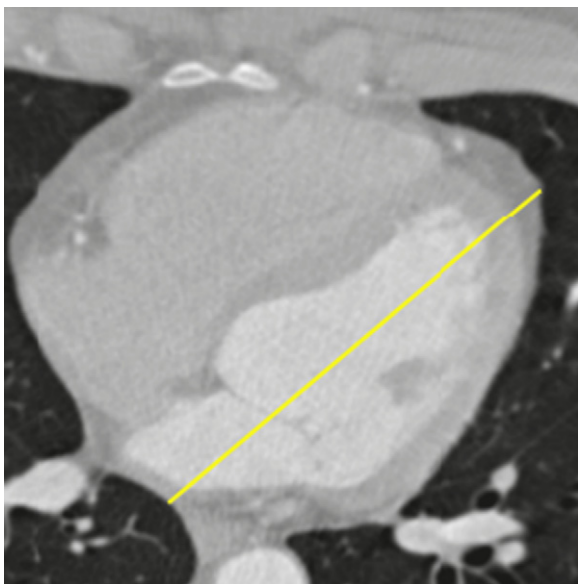


**Fig. 16.** Vertical long axis orientation. It is shown as a line from the cardiac apex through the middle of the mitral valve plane.

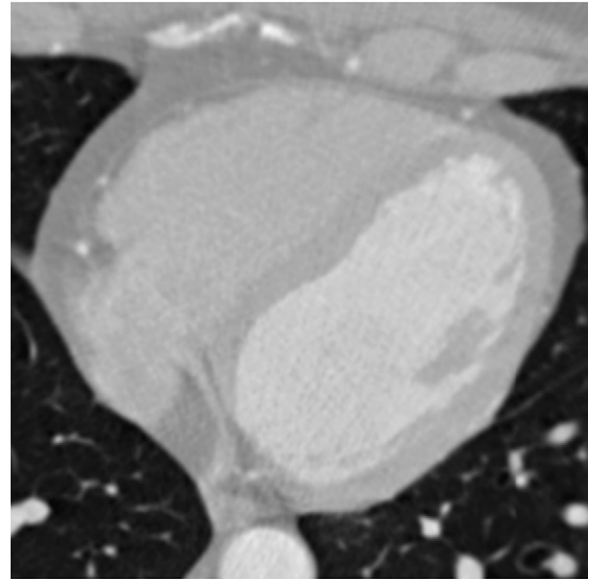
$$\begin{aligned}
& -\alpha \operatorname{div}(\Psi'(|\nabla(u^k+du^{k,l})|^2+|\nabla(v^k+dv^{k,l})|^2) \\
& \nabla(v^k+dv^{k,l+1}))=0 \tag{52}
\end{aligned}$$

### 5.2.2. Multiscale strategy

In order to consider large displacements in our approach we need to include a multiscale strategy [6,2,33,34] that does not contradict the linearization considered in Eqs. (49) and (50).

For the multiresolution strategy a Gaussian pyramid of the image is generated using a downsampling factor  $\eta \in (0,1)$ , where  $\eta$  remains constant for each stage.

a



b

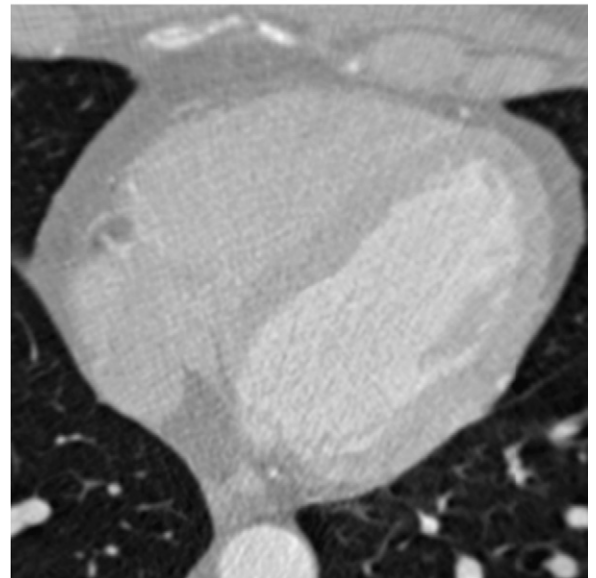


**Fig. 17.** Slice 52 of the CT sequence. (a) 0% of the cardiac cycle. (b) 10% of the cardiac cycle.

The coarse grid is obtained by scaling the images  $L(x,y,t)$  and  $L(x+u,y+v,t+1)$  by a factor  $\eta^i$  for  $i=M-1, M-2, \dots, 0$ , where  $M$  represents the number of decomposition levels.

Starting at the coarse level ( $i=M-1$ ) with  $W^0 = (0,0,1)^T$ ,  $du^{k,0} = 0$  and  $dv^{k,0} = 0$  the inner iteration ( $l$ ) allows obtaining the increment  $du^k$  for the outer iteration ( $k$ ), where  $u^{k+1} = u^k + du^{k,l+1}$  is the solution for the linear system of Eqs. (51) and (52) in the current level [38]. Then, the solution is interpolated and propagate to the next finer level ( $i=i-1$ ) where it is employed for the initialisation of the outer iteration.

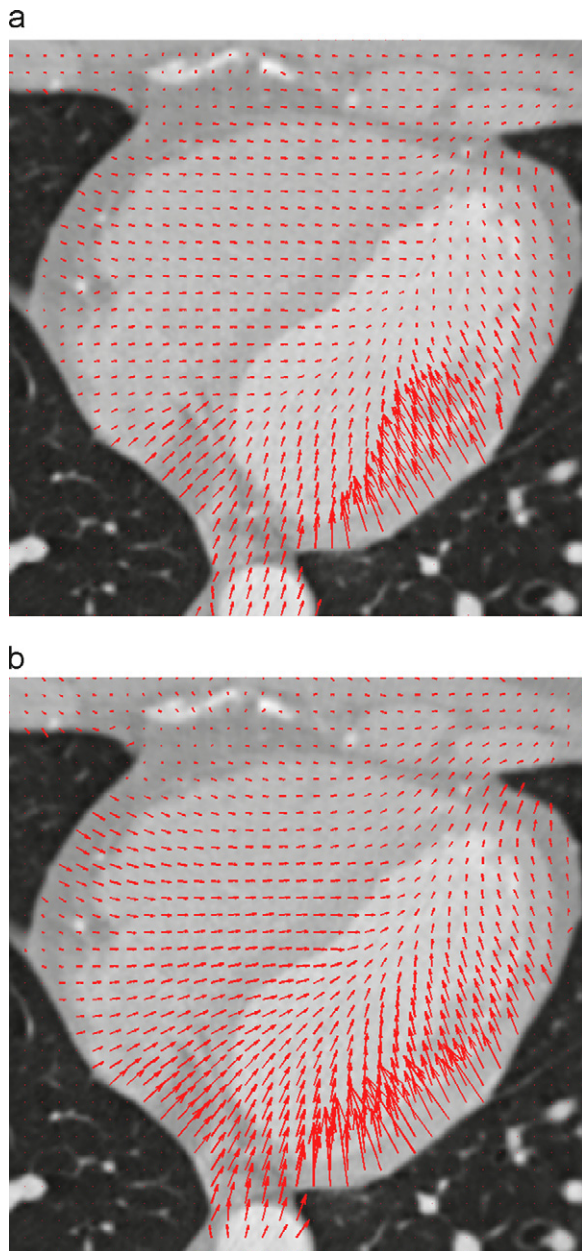


**Fig. 18.** Optical flow of slice 52 of the CT sequence between 0% and 10% of the cardiac cycle. (a) Optical flow algorithm of [38]. (b) Optical flow using steered Hermite transform approach.

## 6. Results

For testing the estimation performance we calculated the angular error from a sequence with ground truth. Since our main goal is to find an estimation method useful to assist diagnosis tasks in CT images, we show objective and subjective tests on this kind of images. In order to perform an objective test on these images we reconstructed sequential images from their adjacent images and their motion vectors. We then measured the backward reconstruction error.

For the optical flow estimation using the steered Hermite transform, we used the parameters of Table 2.

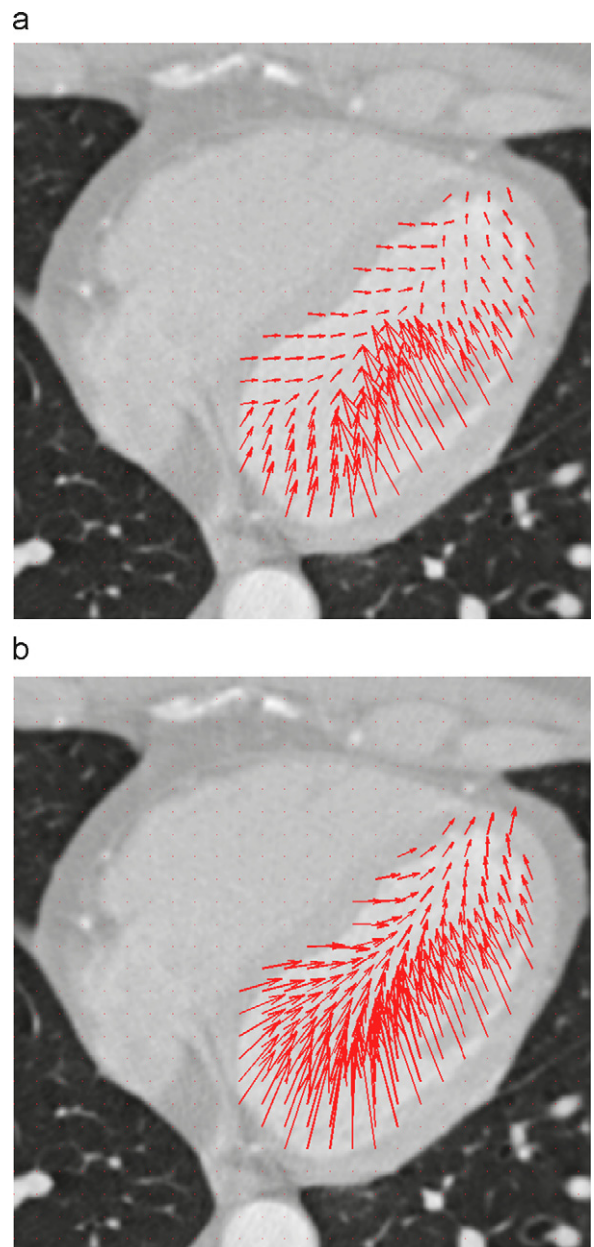


**Fig. 19.** Optical flow left ventricle of slice 52 of the CT sequence between 0% and 10% of the cardiac cycle. (a) Optical flow left ventricle algorithm of [38]. (b) Optical flow left ventricle using steered Hermite coefficients.

### 6.1. Algorithm validation

In order to validate our method we compare our implementation with the 2D algorithm of [38] using the *Dimetrodon* sequence [3].

Fig. 13(a) shows the frame 10 of the *Dimetrodon* sequence and its *ground truth* is displayed in Fig. 13(b). In Fig. 13(c) a reference color wheel is used to encode the direction of the flow vector, where each color represents the direction and its tone the magnitude of the vector.

As a performance measure we calculate the angular error (*AE*) proposed in [3]. The angular error is defined as the angle in 3D space between the dot product of two flow normalized vectors  $\vec{u} = (u_0, u_1)$  and  $\vec{v} = (v_0, v_1)$

$$AE = \arccos(\vec{u} \cdot \vec{v}) \quad (53)$$

where

$$\vec{u} \cdot \vec{v} = u_0 v_0 + u_1 v_1 \quad (54)$$

In Fig. 14 we show the optical flow for the *Dimetrodon* sequence using the approach of [38] (Fig. 14(a)) and the steered Hermite approach (Fig. 14(c)). For the implementation of [38] we used the binaries of the author's website published in [8].

Fig. 14(b) and (d) shows the average error for both approaches, namely  $AE = 3.03^\circ$  for approach [38] and  $AE = 2.7^\circ$  for our proposal. Noting that the error is smaller with our approach.

### 6.2. Optical flow in cardiac CT images

The axial plane is the first image plane in CT and usually gives a good overview of cardiac and coronary anatomy (Fig. 15(a) and (b)). The long vertical axis (Fig. 16) or two-chamber view is easily produced from the axial plane, this corresponds to a vertical plane through the cardiac apex and

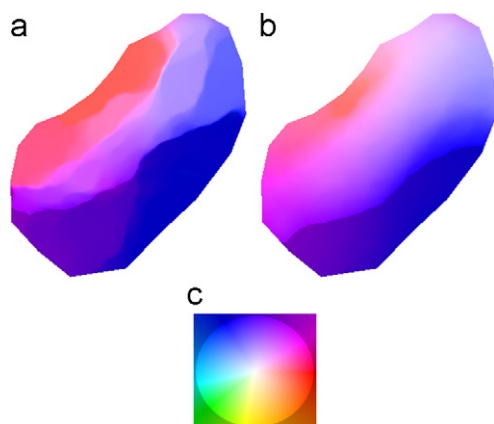


**Fig. 20.** Optical flow left ventricle of slice 52 of the CT sequence between 0% and 10% of the cardiac cycle (color coding). (a) Optical flow left ventricle algorithm of [38] (color coding). (b) Optical flow left ventricle using steered Hermite coefficients (color coding). (c) Reference color wheel.

the center plane of the mitral valve into the left atrium. This view is adequate to delineate the configuration of the left ventricle and to evaluate contraction of the anterior and lower segment of ventricular left myocardium [19].

For the CT images we calculate the flow field of two images taken at different times of the cardiac cycle. The images correspond to the axial plane of cardiac CT and compare our algorithm with the implementation of [38] in 2D.

The strongest cardiac movement is present during contraction of the atria and ventricles in systole, approximately between 0% and 30% of cardiac cycle. This movement is seen

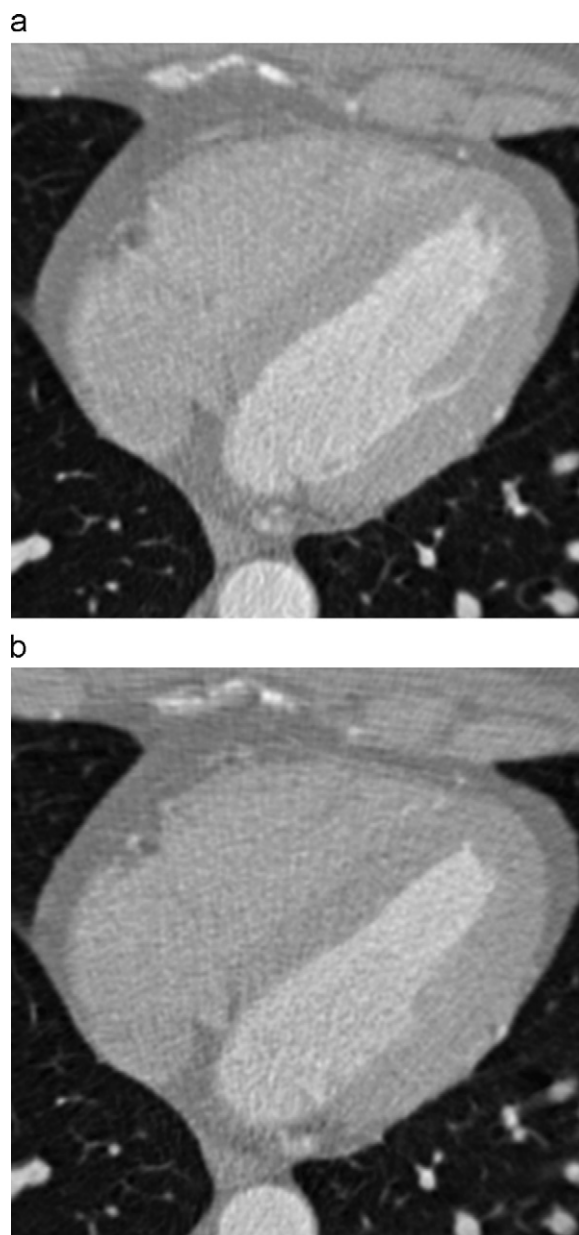


**Fig. 21.** Slice 52 of the CT sequence. (a) 20% of the cardiac cycle. (b) 30% of the cardiac cycle.

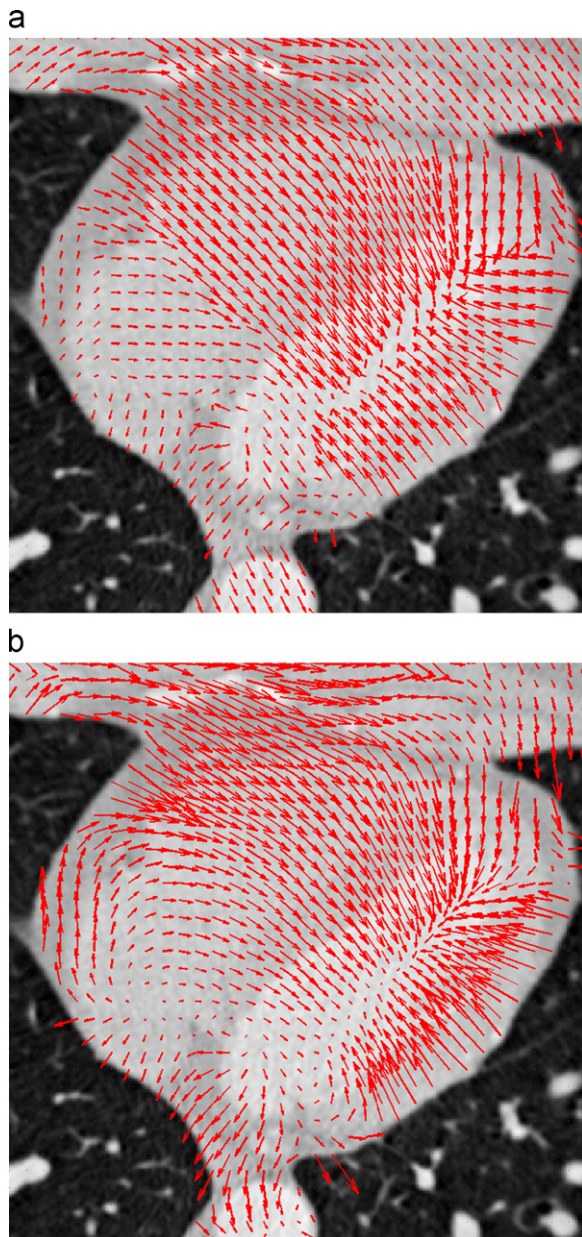


**Fig. 22.** Optical flow of slice 52 of the CT sequence between 20% and 30% of the cardiac cycle. (a) Optical flow algorithm of [38]. (b) Optical flow using steered Hermite transform approach.

in the displacement of the left ventricular wall, the aortic valve flaps, and the different segments of the coronary arteries in representative transaxial planes [37]. Therefore we evaluated the optical flow at different times of the cardiac cycle.

Fig. 17(a) and (b) shows slice 52 of the CT sequence at 0% and 10% of the cardiac cycle (systole), respectively. The resulting optical flow applying the approach of [38] and the steered Hermite transform approach are showing in Fig. 18(a) and (b), respectively.

From a visual evaluation we notice that our algorithm shows clearer and better defined flows especially in areas

close to the cavities, such as the left ventricle, being the study of movement of this structure of major importance to physicians.

Fig. 19 shows the isolated displacements of the left ventricle. For this purpose we use a binarization of the image and apply algorithms of mathematical morphology for a simple segmentation of the left ventricle. Fig. 19(a) shows the optical flow resulting from the algorithm of [38] and Fig. 19(b) the results of the steered Hermite transform algorithm. Due to restrictions used we can determine the optical flow regularized in other areas that not dependent on the textures or artifacts of the images, such as, homogeneous areas that are also of interest for medical diagnosis, despite the noise and the irregular motion of the images used.

In the optical flow field the size of the arrows is proportional to the magnitude of the displacement, which results in an overlap between the vectors. To avoid this we show the velocity field using a color code (Fig. 20). Fig. 20(a) and (b) shows the color code results corresponding to the displacements of Fig. 19.

The left ventricular wall contraction in systole can be seen in Figs. 18–20. In order to show the different movements of cardiac structures, we compute the optical flow at different times of the cardiac cycle. Figs. 22–24 show the estimated optical flow between 20% and 30% corresponding to cardiac cycle of slice 52 shown in Fig. 21, also showing the left ventricular wall contraction.

The movement of relaxation during diastole can be seen between 40% and 60% of the cardiac cycle [37]. Figs. 26–28 show the optical flow between 50% and 60% of cardiac cycle of slice 52 shown in Fig. 25 using both the approach of [38] and the steered Hermite transform. According to [37] the least amount of movement is observed in end-systole and mid- to end-diastole of the cardiac cycle.

### 6.3. Quantitative evaluation of optical flow in cardiac CT images

In order to provide a quantitative measure of our proposal we calculate the Root Mean Squared RMS of the *Backward reconstruction* using the optical flow algorithm of [38] and the steered Hermite coefficients. The computed optical flow for a particular image in a sequence is used to estimate the next image in that sequence. Then the RMS between this estimated image and the actual next image is calculated.

For the reconstruction algorithm we used the *Backward reconstruction* [27]. Let us consider two adjacent images in the CT sequence  $L(x,y,t)$  and  $L(x,y,t+1)$ , and the optical flow  $(u,v)$  between them. Given the values pixels of second image, we can calculate the gray value at  $(x,y)$  in the first image using spline interpolation.

$$\text{RMS error} = \sqrt{\frac{\sum_x \sum_y (L(x,y,t) - \hat{L}(x,y,t))^2}{M * N}} \quad (55)$$

where  $L(x,y,t)$  and  $\hat{L}(x,y,t)$  are the true and reconstructed images of size  $M * N$  at time  $t$ .

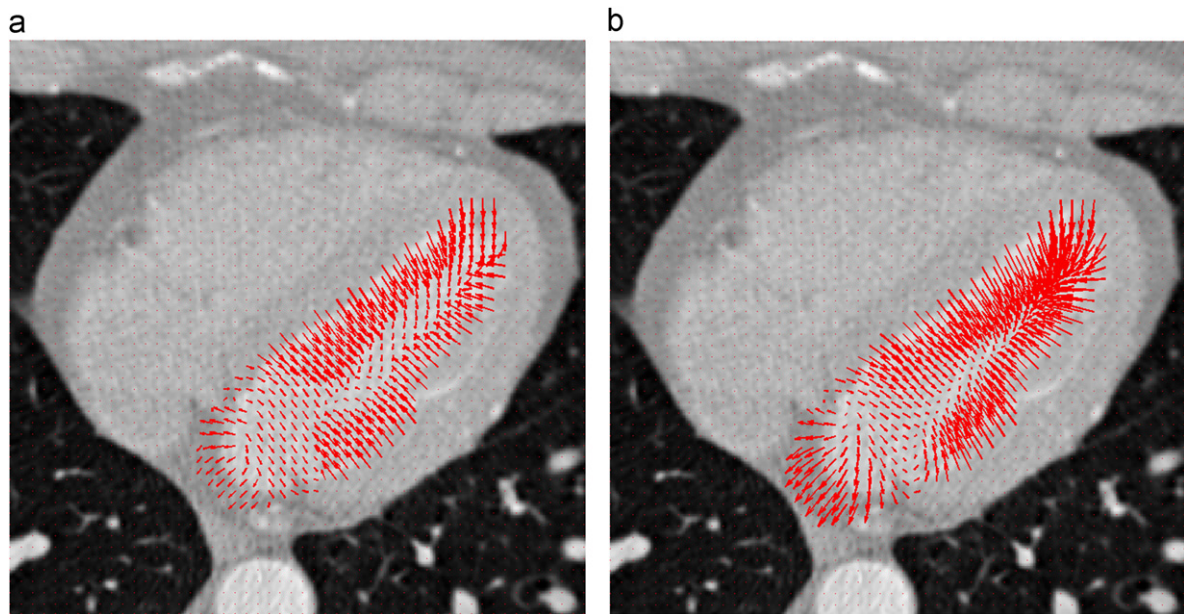
Fig. 29 shows the reconstruction error for the optical flow at 20% of the cardiac cycle of the slice 52 for the approach of [38] and using the steered Hermite coefficients.

Table 3 shows the reconstruction error for the optical flow from 0% to 10%, 20% to 30% and 50% to 60% of the cardiac cycle images of slice 52, first applying the algorithm of [38] and then using the steered Hermite transform.

In Table 3 we note that the RMS error is smaller in our approach, this is because when using the coefficients of order larger than 2 the estimate is more robust to noise. It is important to stress that in spite of the noisy nature of CT images our algorithm has shown accuracy.

## 7. Conclusions

In this paper, we proposed a method of optical flow estimation in cardiac CT images using the steered Hermite transform. The Hermite transform [32,31] is a model that incorporates some of the more important properties of the first stages of the human visual system, such as the overlapping Gaussian receptive fields, the Gaussian derivative model of early vision [52–54], and the multiresolution analysis [16,44]. We have followed a differential



**Fig. 23.** Optical flow left ventricle of slice 52 of the CT sequence between 20% and 30% of the cardiac cycle. (a) Optical flow left ventricle algorithm of [38]. (b) Optical flow left ventricle using steered Hermite coefficients.

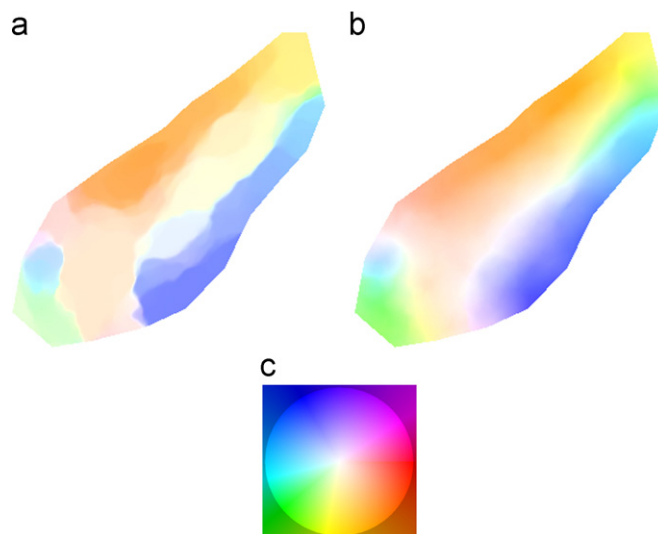


**Fig. 24.** Optical flow left ventricle of slice 52 of the CT sequence between 20% and 30% of the cardiac cycle (color coding). (a) Optical flow left ventricle algorithm of [38] (color coding). (b) Optical flow left ventricle using steered Hermite coefficients (color coding). (c) Reference color wheel.

approach for motion estimation and have included image structure information extracted from the steered Hermite coefficients in the constraint terms of the minimizing function. The advantages of this approach are several. First, using operators based on Gaussian derivatives the spatial scale of analysis becomes a free parameter that can be adjusted to make the algorithm more robust to noise or to analyze spatial objects of different spatial dimensions. We use this feature to build the estimation method on a multiresolution approach,

starting from the lowest resolution. Second, the use of a steered version of the Hermite transform allows the algorithm to analyze perceptually-relevant oriented image structures. Some competitive approaches include a criterion based on the constancy of structures obtained from first-derivative operators but have denied higher order derivatives. Our approach, instead, shows that the inclusion of structures obtained from higher order Gaussian derivatives improves the estimation performance. This means that not only edges are important to

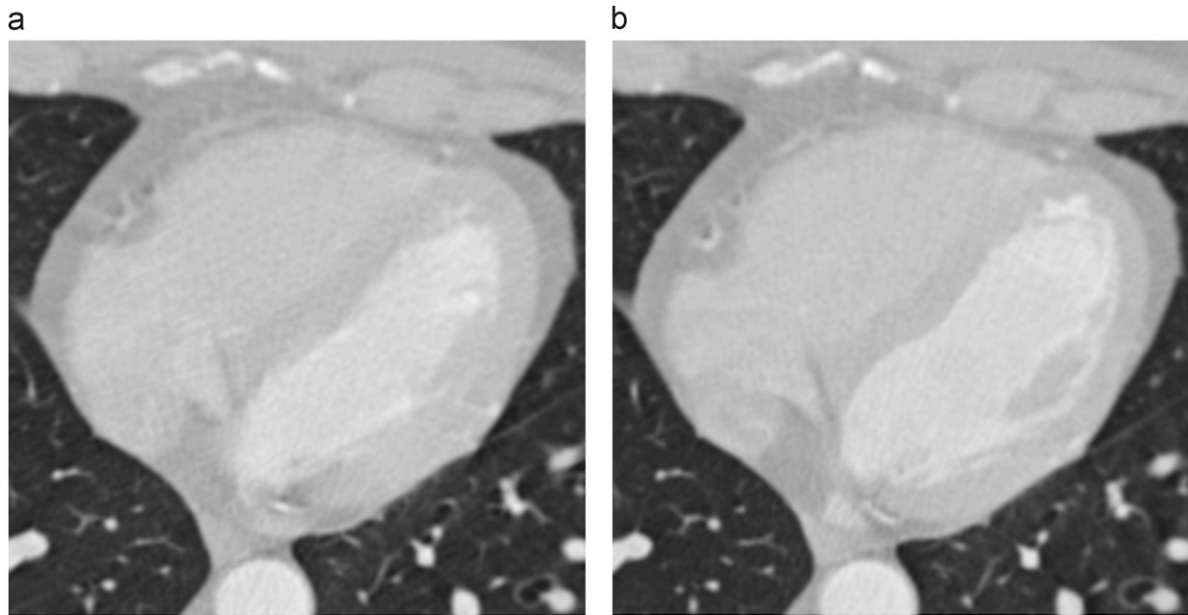


**Fig. 25.** Slice 52 of the CT sequence. (a) 50% of the cardiac cycle. (b) 60% of the cardiac cycle.

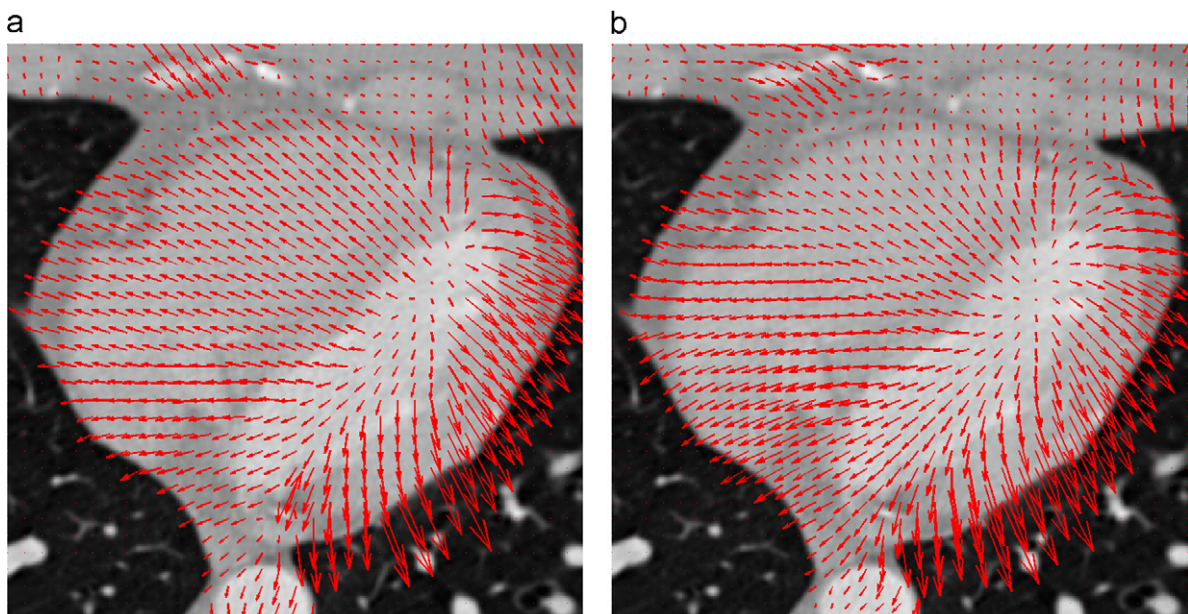


**Fig. 26.** Optical flow of slice 52 of the CT sequence between 50% and 60% of the cardiac cycle. (a) Optical flow algorithm of [38]. (b) Optical flow using steered Hermite transform approach.

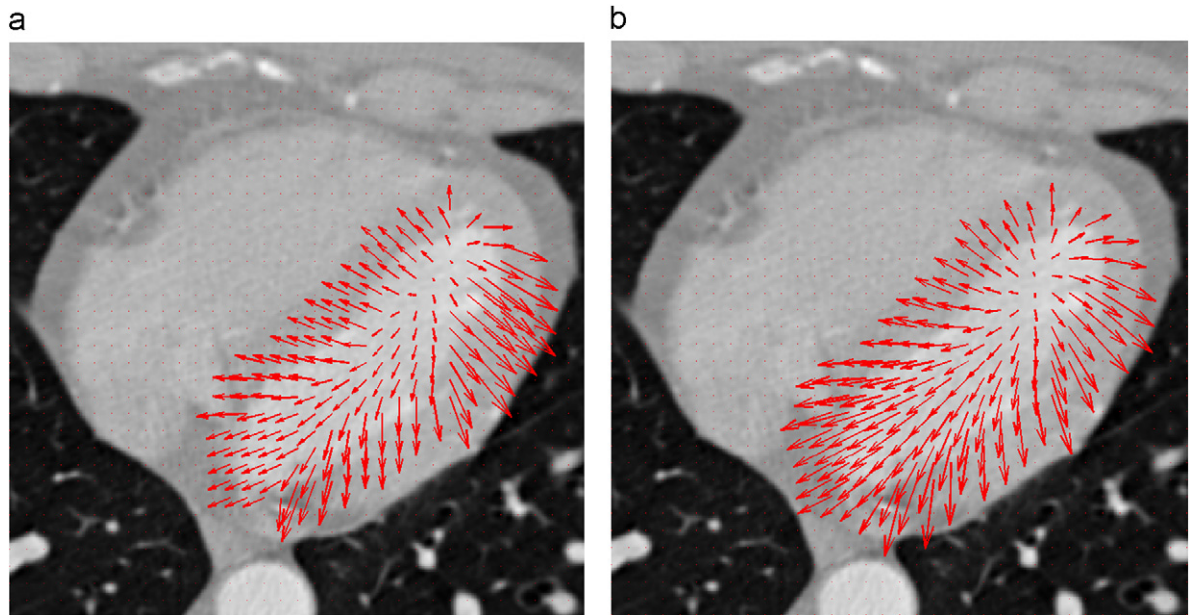


**Fig. 27.** Optical flow left ventricle of slice 52 of the CT sequence between 50% and 60% of the cardiac cycle. (a) Optical flow left ventricle algorithm of [38]. (b) Optical flow left ventricle using steered Hermite coefficients.

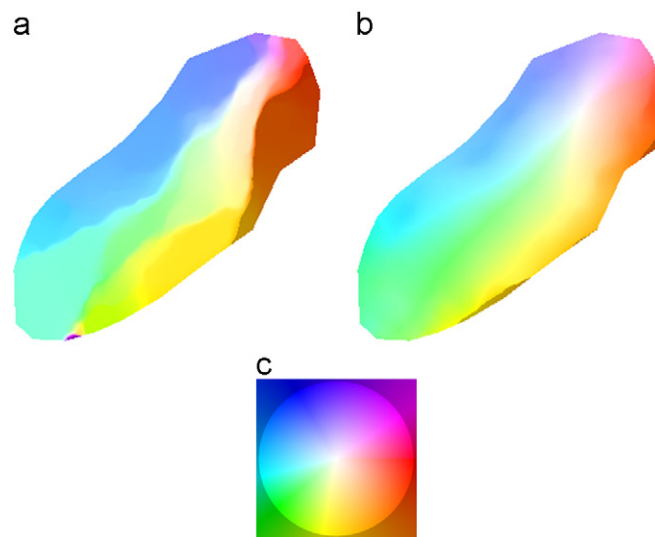


**Fig. 28.** Optical flow left ventricle of slice 52 of the CT sequence between 50% and 60% of the cardiac cycle (color coding). (a) Optical flow left ventricle algorithm of [38] (color coding). (b) Optical flow left ventricle using steered Hermite coefficients (color coding). (c) Reference color wheel.

consider as constancy constraints in the minimizing function but also other oriented image primitives that are obtained with higher Gaussian derivatives. In our approach, the maximum order of the derivative is a free parameter.

Estimation performance has been tested in several ways. Angular error was calculated from a sequence with ground truth and smaller values were found with our method than with a competitive approach. Our main goal is to find an estimation method useful to assist diagnosis tasks in CT images. Therefore we show objective and subjective tests on this kind of images. From a visual

evaluation we notice that our algorithm shows clearer and better defined flows especially in areas close to the cavities, such as the left ventricle, being the study of movement of this structure of major importance to physicians. In order to perform an objective test on these images we reconstructed sequential images from their adjacent images and their motion vectors. We then measured the backward reconstruction error and found smaller errors in our proposal than in competitive approaches. It is important to stress that in spite of the noisy nature of CT images our algorithm has shown accuracy.

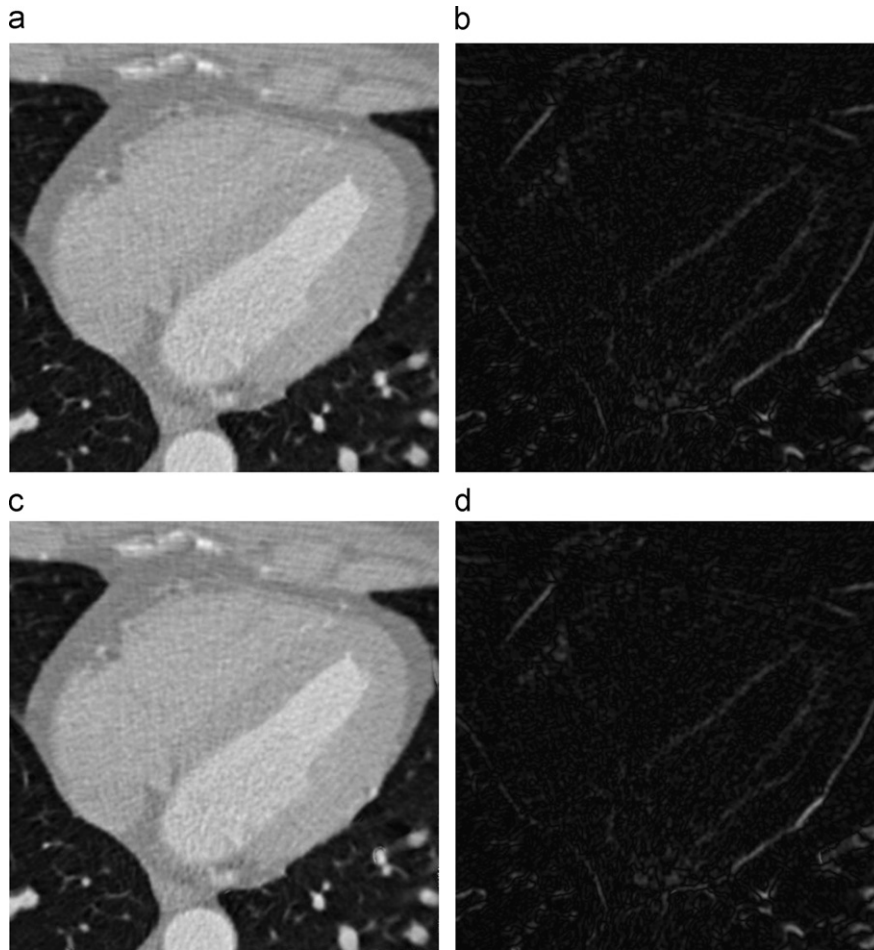


**Fig. 29.** Reconstruction error slice 52 of the CT sequence 20% of the cardiac cycle. (a) *Backward reconstruction* using the optical flow of [38]. (b) Absolute error between the reconstructed first image and the true first image (20% of the cardiac cycle) using approach of [38]. (c) *Backward reconstruction* using the steered Hermite transform. (d) Absolute error between the reconstructed first image and the true first image (20% of the cardiac cycle).

**Table 3**  
Reconstruction RMS error.

% cardiac cycle	RMS error [38]	RMS error Hermite
0–10	28.6214	26.0571
20–30	17.5157	16.9614
50–60	19.5726	19.2855

Using a perceptually relevant image representation model such as the steered Hermite transform we have built a differential motion estimation model that considers perceptually relevant image primitives and not only edges, that is sensitive to locally oriented structure, that incorporates multiresolution analysis and that is robust to noise as is the case of CT images.

**Acknowledgements**

This work was supported by UNAM grants IN113611 and IX100610. E. Moya-Albor thanks to Universidad

Nacional Autónoma de México for the granted doctoral scholarship.

**Appendix A**

The 1D Hermite coefficients are achieved by the inner product between the signal located by the Gaussian window and the Hermite polynomials

$$L_k = \left\langle L(x), H_k \left( \frac{x}{\sigma} \right) \right\rangle = \int_{-\infty}^{\infty} G(x) L(x) H_k \left( \frac{x}{\sigma} \right) dx \tag{A.1}$$

It can be shown that

$$\begin{aligned} L_k &= \left\langle L(x), H_k \left( \frac{x}{\sigma} \right) \right\rangle = \left\langle L^{(1)}(x), H_{k-1} \left( \frac{x}{\sigma} \right) \right\rangle \\ &= \dots = \left\langle L^{(2)}(x), H_{k-2} \left( \frac{x}{\sigma} \right) \right\rangle \\ &= \dots = \left\langle L^{(k)}(x), H_0 \left( \frac{x}{\sigma} \right) \right\rangle \end{aligned} \tag{A.2}$$

where

$$L^{(k)}(x) = \frac{\partial^k L(x)}{\partial x^k}$$

$$H_0\left(\frac{X}{\sigma}\right) = 1 \quad (\text{A.3})$$

Therefore

$$L_k = \langle L^{(k)}(x), 1 \rangle = L^{(k)}(x) \quad (\text{A.4})$$

Eq. (A.4) states that the  $k$ th order Gaussian derivative of the image is the inner product of the image and the  $k$ th order Hermite polynomial [28].

## Appendix B

The Euler–Lagrange equations for Eq. (44) are

$$\begin{aligned} & \Psi'(|L_0(X+W)-L_0(X)|^2 + \gamma|I_{n,\theta}(X+W)-I_{n,\theta}(X)|^2) \\ & \left[ |L_0(X+W)-L_0(X)| \frac{\partial L_0(X+W)}{\partial u(x)} \right. \\ & \left. + \gamma \left( |I_{n,\theta}(X+W)-I_{n,\theta}(X)| \frac{\partial I_{n,\theta}(X+W)}{\partial u(x)} \right) \right] \\ & -\alpha \operatorname{div}(\Psi'(|\nabla u|^2 + |\nabla v|^2)\nabla u) = 0 \end{aligned} \quad (\text{B.1})$$

$$\begin{aligned} & \Psi'(|L_0(X+W)-L_0(X)|^2 + \gamma|I_{n,\theta}(X+W)-I_{n,\theta}(X)|^2) \\ & \left[ |L_0(X+W)-L_0(X)| \frac{\partial L_0(X+W)}{\partial v(y)} \right. \\ & \left. + \gamma \left( |I_{n,\theta}(X+W)-I_{n,\theta}(X)| \frac{\partial I_{n,\theta}(X+W)}{\partial v(y)} \right) \right] \\ & -\alpha \operatorname{div}(\Psi'(|\nabla u|^2 + |\nabla v|^2)\nabla v) = 0 \end{aligned} \quad (\text{B.2})$$

Applying the chain rule for partial derivatives to Eq. (B.1) we get

$$\begin{aligned} \frac{\partial L_0(*)}{\partial u(x)} &= \frac{\partial L_0(*)}{\partial x} \\ \frac{\partial I_{n,\theta}(*)}{\partial u(x)} &= \frac{\partial I_{n,\theta}(*)}{\partial x} \end{aligned} \quad (\text{B.3})$$

from Eq. (A.4) of Appendix A we have that

$$\frac{\partial L_0(X+W)}{\partial x} = L_{1,0}(X+W) \quad (\text{B.4})$$

and

$$\begin{aligned} \frac{\partial I_{n,\theta}(x)}{\partial x} &= \frac{\partial}{\partial x} \sum L_{m,n-m} \cdot g_{m,n-m}(\theta) \\ \frac{\partial I_{n,\theta}(x)}{\partial x} &= \sum L_{(m)+1,n-m} \cdot g_{m,n-m}(\theta) \\ \frac{\partial I_{n,\theta}(x)}{\partial x} &= I_{n,\theta(m)+1}(x) \end{aligned} \quad (\text{B.5})$$

And in a similar way for partial derivatives to Eq. (B.2).

Eqs. (B.4) and (B.5) simplify Eqs. (B.1) and (B.2)

$$\begin{aligned} & \Psi'(|L_0(X+W)-L_0(X)|^2 + \gamma|I_{n,\theta}(X+W)-I_{n,\theta}(X)|^2) \\ & \times [ |L_0(X+W)-L_0(X)| L_{10}(X+W) + \gamma(|I_{n,\theta}(X+W) \\ & -I_{n,\theta}(X)| I_{n,\theta(m)+1}(X+W))] - \alpha \operatorname{div}(\Psi'(|\nabla u|^2 + |\nabla v|^2)\nabla u) = 0 \end{aligned} \quad (\text{B.6})$$

$$\begin{aligned} & \Psi'(|L_0(X+W)-L_0(X)|^2 + \gamma|I_{n,\theta}(X+W)-I_{n,\theta}(X)|^2) \\ & \times [ |L_0(X+W)-L_0(X)| L_{01}(X+W) + \gamma(|I_{n,\theta}(X+W) \\ & -I_{n,\theta}(X)| I_{n,\theta(m)+1}(X+W))] - \alpha \operatorname{div}(\Psi'(|\nabla u|^2 + |\nabla v|^2)\nabla v) = 0 \end{aligned} \quad (\text{B.7})$$

## Appendix C

$$\begin{aligned} & L_0(X+W^{k+1})-L_0(X) \\ & \approx \left( L_0(X+W^k) + du^k \frac{\partial L_0(X)}{\partial x} + dv^k \frac{\partial L_0(X)}{\partial y} \right) - L_0(X) \\ & \approx (L_0(X+W^k) + du^k L_{01}(X) + dv^k L_{10}(X)) - L_0(X) \\ & \approx (L_0(X+W^k) - L_0(X)) + du^k L_{01}(X) + dv^k L_{10}(X) \end{aligned} \quad (\text{C.1})$$

and

$$\begin{aligned} & I_{n,\theta}(X+W^{k+1})-I_{n,\theta}(X) \approx (I_{n,\theta}(X+W^k)-I_{n,\theta}(X)) \\ & + du^k I_{n,\theta(m)+1}(X) + dv^k I_{n,\theta(n)+1}(X) \end{aligned} \quad (\text{C.2})$$

## References

- [1] M. Abramowitz, I. Stegun, Handbook of Mathematical Functions, Dover, New York, 1965.
- [2] P. Anandan, A computational framework and an algorithm for the measurement of visual motion, International Journal of Computer Vision 2 (3) (1989) 283–310.
- [3] S. Baker, D. Scharstein, J.P. Lewis, S. Roth, M.J. Black, R. Szeliski, A database and evaluation methodology for optical flow, in: IEEE International Conference on Computer Vision, 2007, pp. 1–8.
- [4] J. Barron, D. Fleet, S. Beauchemin, Performance of optical flow techniques, International Journal of Computer Vision 12 (1994) 43–77.
- [5] J. Bigün, G. Granlund, J. Wilklund, Multidimensional orientation estimation with applications to texture analysis and optical flow, IEEE Transactions on Pattern Analysis and Machine Intelligence 13 (8) (1991) 775–790.
- [6] M.J. Black, P. Anandan, The robust estimation of multiple motions: parametric and piecewise-smooth flow fields, Computer Vision and Image Understanding 63 (1) (1996) 75–104.
- [7] J. Bloom, T. Reed, A gaussian derivative-based transform, IEEE Transactions on Image Processing 5 (March (3)) (1996) 551–553.
- [8] T. Brox, Classical Variational optical Flow, 2011 <http://lmb.infor.matik.uni-freiburg.de/resources/binaries> (accessed 10.12.11).
- [9] A. Bruhn, J. Weickert, Towards ultimate motion estimation: combining highest accuracy with real-time performance, in: Proceedings of the Tenth IEEE International Conference on Computer Vision, vol. 1, IEEE Computer Society Press, 2005, pp. 749–755.
- [10] A. Bruhn, J. Weickert, C. Feddern, T. Kohlberger, C. Schnörr, Variational optical flow computation in real time, IEEE Transactions on Image Processing 14 (April (5)) (2005) 608–615.
- [11] A. Bruhn, J. Weickert, C. Schnörr, Combining the advantages of local and global optic flow methods, in: Proceedings of the Twenty-fourth DAGM Symposium on Pattern Recognition, Springer-Verlag, London, UK, 2002, pp. 454–462.
- [12] A. Bruhn, J. Weickert, C. Schnörr, Lucas/kanade meets horn/schunck: combining local and global optic flow methods, International Journal of Computer Vision 61 (2005) 211–231.
- [13] G. Buckberg, J.I. Hoffman, A. Mahajan, S. Saleh, C. Coghlan, Cardiac mechanics revisited: the relationship of cardiac architecture to ventricular function, Circulation 118 (24) (2008) 2571–2587.
- [14] F. Cademartiri, G. Luccichentia, A. van Der Lugt, P. Pavone, P.M. Pattynama, P.J. de Feyter, G.P. Krestin, Sixteen-row multislice computed tomography: basic concepts, protocols, and enhanced clinical applications, Seminars in Ultrasound, CT and MRI 25 (February (1)) (2004) 2–16.
- [15] P. Charbonnier, L. Blanc-Féraud, G. Aubert, M. Barlaud, Two deterministic half-quadratic regularization algorithms for computed imaging, in: International Conference on Image Processing, vol. 2, IEEE Computer Society Press, 1994, pp. 168–172.
- [16] B. Escalante-Ramírez, J.L. Silván-Cárdenas, Advanced modeling of visual information processing: a multiresolution directional-oriented image transform based on gaussian derivatives, Signal Processing: Image Communication 20 (9–10) (2005) 801–812.
- [17] B. Escalante-Ramírez, J.L. Silván-Cárdenas, H. Yuen-zhou, Optic flow estimation using the hermite transform, in: Proceedings of the SPIE

- in Applications of Digital Image Processing XXVII, vol. 5558, 2004, pp. 632–643.
- [18] A. Estudillo-Romero, B. Escalante-Ramírez, Rotation-invariant texture features from the steered hermite transform, *Pattern Recognition Letters* 32 (16) (2011) 2150–2162.
- [19] R. Fischbach, Cardiac and cardi thoracic anatomy in CT, in: *Multi-slice and Dual-source CT in Cardiac Imaging*, 2nd ed., Springer, Berlin/Heidelberg, 2007, pp. 23–39.
- [20] W.T. Freeman, E.H. Adelson, The design and use of steerable filters, *IEEE Transactions on Pattern Analysis and Machine Intelligence* 13 (1991) 891–906.
- [21] B. Galvin, B. Mccane, K. Novins, D. Mason, S. Mills, Recovering motion fields: an evaluation of eight optical flow algorithms, in: *British Machine Vision Conference*, 1998, pp. 195–204.
- [22] J.J. Gibson, The perception of the visual world, *The American Journal of Psychology* 64 (October) (1951) 622–625.
- [23] J.J. Gibson, *The Senses Considered as Perceptual Systems*, Houghton Mifflin Company, 1966.
- [24] B.K. Horn, B.G. Schunck, Determining optical flow, *Artificial Intelligence* 17 (1–3) (1981) 185–203.
- [25] J. Koenderink, A. van Doorn, Generic neighborhood operators, *IEEE Transactions on Pattern Analysis and Machine Intelligence* 14 (6) (1992) 597–605.
- [26] M.D. Levine, *Vision in Man and Machine*, McGraw-Hill, 1985.
- [27] T. Lin, J.L. Barron, Image reconstruction error for optical flow, in: *Vision Interface*, May 2002, pp. 73–80.
- [28] H. Liu, T.-H. Hong, M. Herman, R. Chellappa, A general motion model and spatio-temporal filters for computing optical flow, *International Journal of Computer Vision* 22 (1997) 141–172.
- [29] B.D. Lucas, T. Kanade, An iterative image registration technique with an application to stereo vision, in: *Proceedings of the Seventh International Joint Conference on Artificial Intelligence (IJCAI '81)*, April 1981, pp. 674–679.
- [30] D. Marr, E. Hildreth, A theory of edge detection, *Proceedings of the Royal Society of London B* 207 (1980) 187–217.
- [31] J. Martens, The hermite transform-applications, *IEEE Transactions on Acoustics, Speech and Signal Processing* 38 (9) (1990) 1607–1618.
- [32] J. Martens, The hermite transform-theory, *IEEE Transactions on Acoustics, Speech and Signal Processing* 38 (9) (1990) 1595–1606.
- [33] E. Mémin, P. Pérez, A multigrid approach for hierarchical motion estimation, in: *ICCV '98: Proceedings of the Sixth International Conference on Computer Vision*, IEEE Computer Society, Washington, DC, USA, 1998, pp. 933–938.
- [34] E. Mémin, P. Pérez, Hierarchical estimation and segmentation of dense motion fields, *International Journal of Computer Vision* 46 (2) (2002) 129–155.
- [35] H.-H. Nagel, Constraints for the estimation of displacement vector fields from image sequences, in: *International Joint Conference on Artificial Intelligence*, 1983, pp. 945–951.
- [36] H.-H. Nagel, W. Enkelmann, An investigation of smoothness constraints for the estimation of displacement vector fields from image sequences, *Pattern Analysis and Machine Intelligence* 8 (September (5)) (1986) 565–593.
- [37] B. Ohnesorge, T. Flohr, Principles of multi-slice cardiac ct imaging, in: *Multi-slice and Dual-source CT in Cardiac Imaging*, 2nd ed., Springer, Berlin/Heidelberg, 2007, pp. 71–126.
- [38] N. Papenberg, A. Bruhn, T. Brox, S. Didas, J. Weickert, Highly accurate optic flow computation with theoretically justified warping, *International Journal of Computer Vision* 67 (April (2)) (2006) 141–158.
- [39] R. Rodieck, Quantitative analysis of cat retinal ganglion cell response to visual stimuli, *Vision Research* 5 (12) (1965) 583–601.
- [40] B. Sakitt, H. Barlow, A model for the economical encoding of the visual image in cerebral cortex, *Biological Cybernetics* 43 (2) (1982) 97–108.
- [41] P. Schoenhagen, A.E. Stillman, S.S. Halliburton, R.D. White, CT of the heart: principles, advances, clinical uses, *Cleveland Clinic Journal of Medicine* 72 (2) (2005) 127–140.
- [42] U. Schoepf, C. Becket, L. Hofmann, E. Yucel, Multidetector-row CT of the heart, *Radiologic Clinics of North America* 41 (3) (2003) 491–505.
- [43] J.L. Silván-Cárdenas, B. Escalante-Ramírez, Optic-flow information extraction with directional gaussian-derivatives, in: *Proceedings of the International Conference on Pattern Recognition*, vol. 3, IEEE Computer Society, Washington, DC, USA, 2000, p. 3194.
- [44] J.L. Silván-Cárdenas, B. Escalante-Ramírez, The multiscale hermite transform for local orientation analysis, *IEEE Transactions on Image Processing* 15 (5) (2006) 1236–1253.
- [45] G. Szegő, *Orthogonal Polynomials*, Colloquium Publications, American Mathematical Society, 1959.
- [46] C. Tomasi, R. Manduchi, Bilateral filtering for gray and color images, in: *Proceedings of the Sixth International Conference on Computer Vision (ICCV '98)*, IEEE Computer Society, Washington, DC, USA, 1998, pp. 839–846.
- [47] S. Uras, F. Girosi, A. Verri, V. Torre, A computational approach to motion perception, *Biological Cybernetics* 60 (1988) 79–87.
- [48] A. van Dijk, J. Martens, Image representation and compression with steered hermite transforms, *Signal Processing* 56 (1) (1997) 1–16.
- [49] R. van Rullen, S.J. Thorpe, Rate coding versus temporal order coding: what the retinal ganglion cells tell the visual cortex, *Neural Computation* 13 (6) (2001) 1255–1283.
- [50] R. Wilson, G.H. Granlund, The uncertainty principle in image processing, *IEEE Transactions on Pattern Analysis and Machine Intelligence* 6 (November (6)) (1984) 758–767.
- [51] J. Xiao, H. Cheng, H. Sawhney, C. Rao, M. Isnardi, S. Corporation, Bilateral filtering-based optical flow estimation with occlusion detection, in: *European Conference on Computer Vision (ECCV)*, 2006, pp. 211–224.
- [52] R. Young, *The Gaussian Derivative Theory of Spatial Vision: Analysis of Cortical Cell Receptive Field Line-weighting Profiles*, Technical Report, General Motors Res Labs, 1985.
- [53] R. Young, Simulation of human retinal function with the gaussian derivative model, in: *Proceedings of the IEEE Conference on Computer Vision and Pattern Recognition*, 1986, pp. 564–569.
- [54] R. Young, The gaussian derivative model for spatial vision: I. Retinal mechanisms, *Spatial Vision* 2 (4) (1987) 273–293.